EUROPEAN ORGANIZATION FOR NUCLEAR RESEARCH

CERN-EP-2019-020
8 February 2019

Calibration of the photon spectrometer PHOS of the ALICE experiment

ALICE Collaboration*

Abstract

The procedure for the energy calibration of the high granularity electromagnetic calorimeter PHOS of the ALICE experiment is presented. The methods used to perform the relative gain calibration, to evaluate the geometrical alignment and the corresponding correction of the absolute energy scale, to obtain the nonlinearity correction coefficients and finally, to calculate the time-dependent calibration corrections, are discussed and illustrated by the PHOS performance in proton-proton (pp) collisions at $\sqrt{s} = 13$ TeV. After applying all corrections, the achieved mass resolution of π^0 and η mesons for $p_{\mathrm{T}} > 1.7$ GeV/c is $\sigma_m^{\pi^0} = 4.56 \pm 0.03$ MeV/c^2 and $\sigma_m^{\eta} = 15.3 \pm 1.0$ MeV/c^2.

*See Appendix A for the list of collaboration members

1 Introduction

The ALICE experiment [1] is one of the four major experiments at the Large Hadron Collider (LHC) at CERN. Its primary goal is the study of the properties of the hot and dense quark–gluon matter created in ultrarelativistic heavy-ion collisions. This dictates the unique features of the ALICE detector design: ability to register and identify both soft particles, reflecting collective behavior of the hot matter, and hard penetrating probes, i.e. jets, direct photons, etc., carrying information about the inner, hottest part of the created fireball. The ALICE experiment incorporates detectors based on all available particle identification techniques. Its tracking system is able to detect and identify relatively soft charged particles with transverse momentum $p_{\mathrm{T}} > 50-100$ MeV/c and process high-multiplicity events. ALICE includes an electromagnetic calorimeter system: the PHOton Spectrometer (PHOS) [1, 2] and the Electromagnetic Calorimeter (EMCal) [3] with the Di-Jet Calorimeter (DCal) [4]. The PHOS calorimeter is designed to measure spectra, collective flow and correlations of thermal and prompt direct photons, and of neutral mesons via their decay into photon pairs. This requires high granularity as well as excellent energy and position resolution. The primary physics goal of the electromagnetic calorimeter EMCal/DCal is the measurement of electrons from heavy flavour decays and the electromagnetic component of jets, spectra and correlations of isolated direct photons and spectra of neutral mesons. This goal dictates a large acceptance but less strict requirements on the energy and position resolution. In this paper, the methods used for the calibration of the PHOS detector during the LHC data taking campaigns of 2009−2013 (Run 1) and 2015−2017 (Run 2) are described and results of the calibration are presented.

The procedure for electromagnetic calorimeter calibration, developed by high-energy experiments, depends on physics objectives, detector resolution, beam availability and hardware implementation of the calorimeters and their front-end electronics. The four LHC experiments use different approaches: the electromagnetic calorimeter (ECAL) of the LHCb experiment [5] was pre-calibrated with the energy flow method, requiring the transverse energy distribution over the calorimeter to be a smooth function of the coordinates, and fine calibrated using the π^0 peak with two approaches: using invariant mass distributions and minimizations of event-by-event variables [6, 7]. The electromagnetic calorimeter (ECAL) of the CMS experiment [8] was pre-calibrated with laboratory measurements of crystal light yield and photodetector gain, followed by beam tests with high-energy electrons and cosmic-ray muons. The final result was obtained with an absolute calibration determined by using the Z-boson mass and channel-by-channel relative calibration using three different methods: the calibration of the transverse energy (by exploiting φ-symmetry), the π^0 and η meson invariant mass fit and the comparison of the energy measured with the ECAL with the track momentum measured by the silicon tracker for isolated electrons from W^- and Z-boson decays [9, 10]. The longitudinally segmented liquid-argon calorimeter of the ATLAS experiment [11] was calibrated by a simulation-based e/γ response using a multivariate algorithm [12]. The absolute energy scale of electrons was calibrated using a large sample of $Z \to e^+e^-$ decays and validated with $J/\psi \to e^+e^-$ decays.

The energy calibration of PHOS includes four mutually dependent aspects: relative gain calibration, absolute energy calibration, nonlinearity correction, and time-dependent calibration correction. The PHOS detector will be briefly described in section 2. The relative gain calibration is presented in section 3, including the pre-calibration using the LED monitoring system and the calibration using the π^0 peak position which are described in sections 3.2 and 3.3, respectively. Fixing the absolute energy calibration of a calorimeter using the π^0 mass peak suffers from systematic uncertainties due to the geometrical alignment of the calorimeter and the energy scale. Because of that the absolute energy calibration is validated using the electron E/p ratio, as described in section 4.1, and the detector geometrical alignment is checked as described in section 4.2. The estimation of the nonlinearity correction is described in section 5 and the calculation of the time-dependent energy calibration correction is discussed in section 6. The final calibration results are presented in section 7.

2 Setup

The PHOS is a single arm, high-resolution electromagnetic calorimeter which detects and identifies photons and electrons in a wide p_{T} range from $\sim$ 100 MeV/c to $\sim$ 100 GeV/c at mid-rapidity and, additionally, provides a trigger in case of a large energy deposition by an energetic particle. The main parameters of the detector are summarized in Tab. 1. PHOS is subdivided into four independent units, named modules, positioned at the bottom of the ALICE detector at a radial distance of 460 cm from the interaction point to the front surface of crystals as shown in Fig. 1. It covers approximately a quarter of a unit in pseudo-rapidity, $|\eta| \leq 0.125$, and 70° in azimuthal angle. Its total active area is 6 m^2.

Table 1: General parameters of the PHOS detector

Coverage in pseudo-rapidity	$-0.125 \leq \eta \leq 0.125$
Coverage in azimuthal angle	$\Delta\varphi = 70°$
Distance to interaction point	460 cm
Modularity	Three modules with 3584 and one with 1792 crystals
Material	Lead-tungstate ($PbWO_4$) crystals
Crystal dimensions	$22 \times 22 \times 180$ mm^3
Depth in radiation length	20 X_0
Number of crystals	12 544
Total area	6.0 m^2
Operating temperature	$-25°$ C

Three PHOS modules are segmented into 3584 detection elements (cells) arranged in 56 rows of 64 elements each, while the fourth module has 56 rows of 32 elements. A fragment of a cell matrix is shown in Fig. 2, left. The PHOS modules are numbered from 1 to 4 counterclockwise [1]. Each element is made of a $22 \times 22 \times 180$ mm^3 lead-tungstate crystal, $PbWO_4$, coupled to a 5×5 mm^2 Avalanche PhotoDiode (APD) whose signal is processed by a low-noise preamplifier. The APD and the preamplifier are integrated in a common body glued onto the end face of the crystal with optically transparent glue with a high refractive index, see Fig. 2, right. The $PbWO_4$ was chosen as an active medium because it is a dense, fast and relatively radiation-hard scintillating crystal. Its radiation length is only 0.89 cm and its Molière radius is 2.0 cm. It has a broad emission spectrum with bands around 420 and 550 nm [13].

The light yield of $PbWO_4$ crystals is relatively low and strongly depends on temperature (temperature coefficient of $-2\%/°$C). In order to increase it by about a factor 3 compared to normal conditions, the PHOS crystals are operated at a temperature of $-25°$C. The energy resolution of a PHOS prototype measured under these conditions in beam tests [14] is described by a parametrization as follows

$$\frac{\sigma_E}{E} = \sqrt{\left(\frac{a}{E}\right)^2 + \left(\frac{b}{\sqrt{E}}\right)^2 + c^2} \tag{1}$$

where $a = 0.013$ GeV, $b = 0.0358$ GeV$^{1/2}$ and $c = 0.0112$. The temperature of the $PbWO_4$ crystals is stabilized with a precision of 0.3°C. Temperature monitoring is based on resistive temperature sensors of thickness $30-50$ μm inserted in the gap between the crystals. For the purpose of temperature stabilization, a PHOS module is subdivided by thermo-insulation into "cold" and "warm" volumes. Detection elements are mounted into the main mechanical assembly units of a module, the so called strip unit, which consists of two rows of eight elements each. The crystal strips are located in the cold volume, whereas the readout electronics is located outside, in the warm volume. The APDs belonging to one strip unit and associated preamplifiers provide 2×8 analog signals to a T-shaped connector which passes the signals from the cold zone to the front-end and trigger electronics located in the warm zone. All six sides of the cold volume are equipped with cooling panels. The heat is removed by a liquid coolant (perfluorohexane, C_6F_{14}) circulating through the pipes on the inner panel surfaces. Moisture condensation is prevented by making airtight cold and warm volumes ventilated with nitrogen.

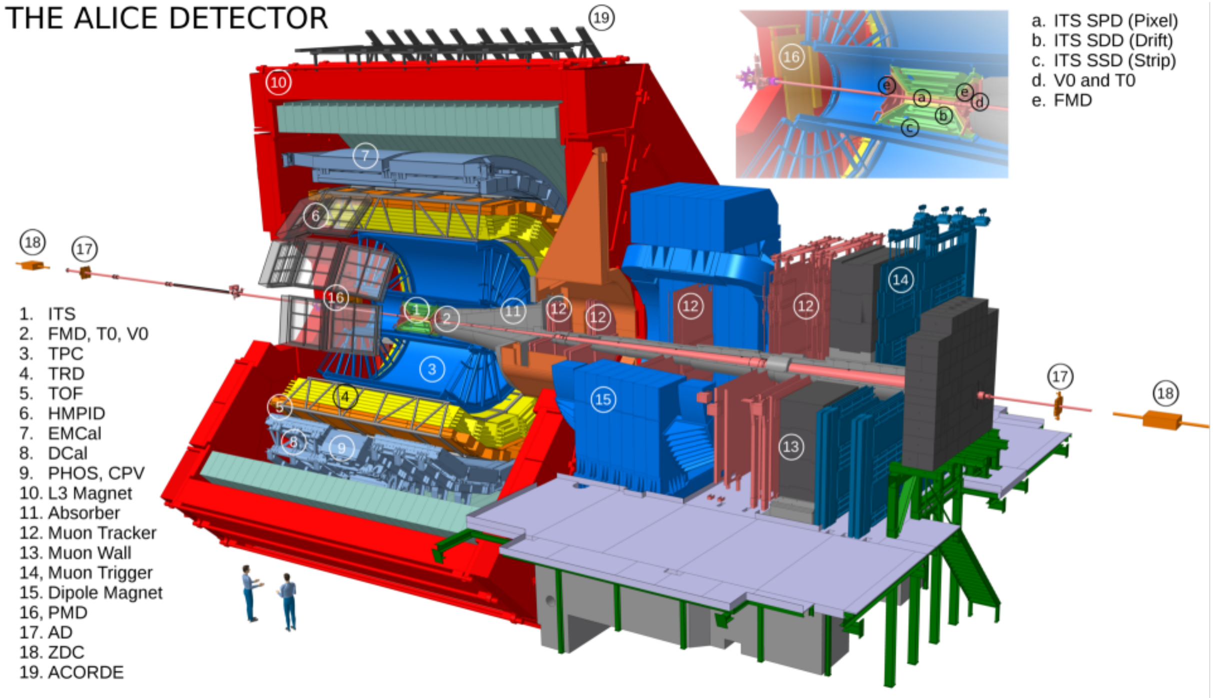

Figure 1: [Color online] ALICE setup, PHOS modules are located at the bottom of the setup.

The monitoring system with LEDs and stable current generators allows every PHOS detection channel to be monitored [15]. The system consists of LED matrices for each PHOS module, having one LED per PHOS cell with controlled light amplitude and flashing rate.

The PHOS electronic chain includes energy digitization and trigger logic for generating trigger inputs to the zero (L0) and first (L1) levels of the ALICE Central Trigger Processor (CTP) [16]. In order to cover the required large dynamic range from 10 MeV to 100 GeV, each energy shaper channel provides two outputs with low and high amplification, digitized in separate ADCs. The upper limit of the dynamic ranges in high- and low-gain channels are 5 GeV and 80 GeV, with the ratio of these amplifications varying slightly from channel to channel with a mean of approximately 16.8. The voltage distribution and control system allows the gain of each APD to be tuned by setting the bias voltage individually. To equalize the energy response of all cells, the APD bias control system allows one to adjust the bias

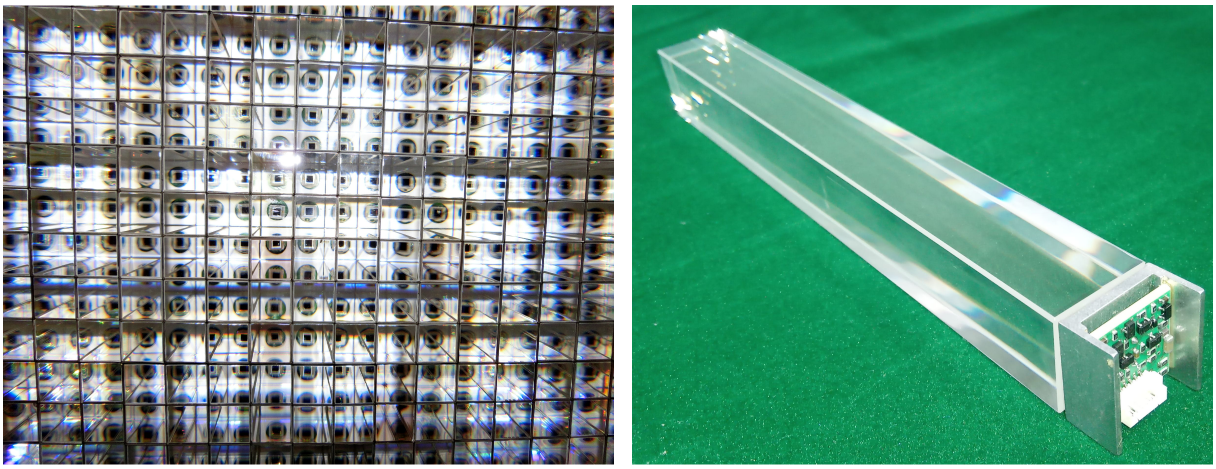

Figure 2: [Color online] Left: fragment of a cell matrix of one module; Right: crystal detector with photodetector and preamplifier.

voltage of each APD with an accuracy of 0.2 V, which corresponds to a $\sim 0.5\%$ gain variation (see Fig. 5, left for more details). The timing information is derived from an offline pulse-shape analysis.

3 Energy calibration procedure

Photons and electrons hitting an electromagnetic calorimeter produce electromagnetic showers with a transverse profile determined by the Molière radius of the calorimeter material. When the transverse cell size of the calorimeter is comparable with the Molière radius, such as in PHOS, the electromagnetic shower is developed in several adjacent cells around the impact point. The group of cells with common edges, containing the electromagnetic shower generated by a photon, is referred to as a cluster (see sec. 4.5.2 of [2]), and the sum of energies deposited by the shower in each cell of the cluster, is the measured photon energy [17]. With the PHOS granularity, the energy deposited in the central cell of the cluster is about 80% of the total cluster energy.

However, in real conditions, the amplitude of signals measured in the cells of the cluster, is proportional to the deposited energy in the cells, up to an unknown calibration constant. Relative energy calibration means equalization of the response of all channels to the same energy deposition. In the case of PHOS, calibration at the hardware level via adjusting the APD bias voltage is complemented by refinement of the calibration parameters in an offline analysis. The adjustment of amplification in all channels is important in order to make the threshold of the trigger efficiency response turn-on curve as sharp as possible which ensures uniformity of the trigger response over the PHOS acceptance. This adjustment was performed once during the PHOS commissioning in LHC Run 1 and another time before the start of the LHC Run 2 data taking period. The final calibration is done in an offline analysis described hereafter in detail. In order to disentangle calibration effects from effects related to cluster overlaps in the high occupancy environment of heavy-ion collisions, the calibration should be performed in low occupancy events provided by pp collisions.

At first, two approaches were tested: calibration using the Minimum-Ionizing Particle (MIP) peak and equalization of mean energies in each channel. The minimum ionization signal of charged particles in the PHOS detector has a most probable value of about 250 MeV which is rather small so that the contribution of electronics noise to the MIP signal is not negligible and the width of the MIP peak $\sigma_{\rm MIP} = 25$ MeV is relatively large, which limits the accuracy of the relative calibration using the MIP peak to a comparable calibration accuracy of a few tens of percent using the APD gain adjustment. The second method based on the mean energy equalization has a poor convergence of iterative calculation of the calibration parameters, especially without pre-calibration using the APD gain adjustment: the mean energy strongly depends on the range of averaging which, in turn, depends on the initial calibration, which results in large uncertainties on the calibration parameters. Nevertheless, this method was used to provide a reasonable calibration for the first measurement of neutral meson spectra in 2010 [18], when the accumulated statistics was not sufficient for more precise methods. Later, a more precise calibration based on the π^0 peak equalization described below was deployed in all subsequent papers [19–23].

Our final strategy of the PHOS relative calibration is based on APD gain equalization as a pre-calibration (see section 3.2) and the π^0 peak adjustment as a final step (see section 3.3).

3.1 Gain ratio calibration

The ratio of high-to-low gain is defined by the electronics components of the amplifiers and may vary from channel to channel. Therefore it is considered as one of the calibration parameters to be determined. The calibration methods discussed in the section 3.3 of this paper are based on data collected with beam, and ensure a good calibration of high-gain channels within the high-gain dynamic range, $E < 5$ GeV. Low-gain channels can hardly be calibrated with the π^0 peak adjustment method described in section 3.3, because of the limited statistics of high-energy clusters. Therefore the ratio of high-to-low gain has to

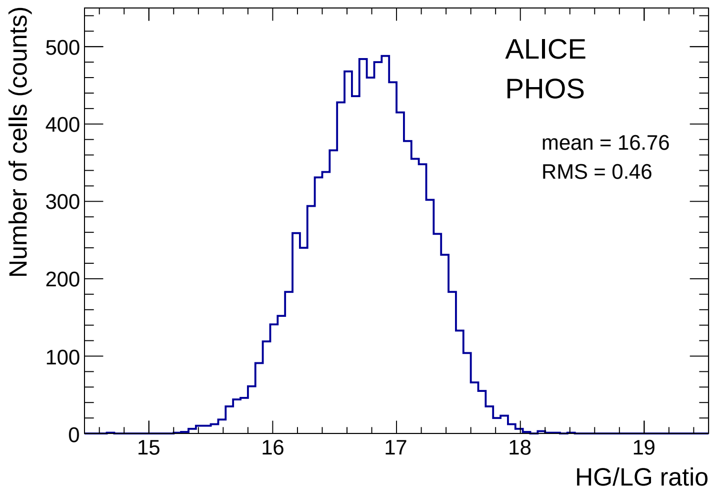

Figure 3: Ratio of high-to-low gain in all cells.

be measured independently using signals of amplitudes which are detected simultaneously in both high- and low-gain channels. The LED monitoring system with its capability to emit signals at high rate with variable amplitudes in the whole dynamic range of PHOS, was used to measure the high-to-low gain ratio. The gain ratio distribution for all active PHOS cells is shown in Fig. 3 and spans from 15 to 18 with an average of about 16.8. The obtained gain ratio is used for high energy amplitudes exceeding the high-gain dynamic range. In this case, the energy is calculated by multiplication of the measured amplitude by a product of high-gain calibration parameter and the high-to-low gain ratio. The high-to-low gain ratio is stable and thus does not need to be frequently measured and updated.

3.2 Photodetector gain equalization

The gain of the PHOS photodetectors, APDs, depends on the bias voltage applied to them. Each APD has its individual gain-voltage characteristic. At the lowest bias voltage, the APD gain is assumed to be equal to one, then it increases with the bias voltage. The APD gain is calculated as the ratio of the measured amplitude at a given voltage to a reference amplitude at 20 V where the dark current in the APD is negligible. The dependence of the APD gain on the bias voltage was measured using the PHOS LED monitoring system, whose programmable light output was tested to be very stable over several hours, a period far longer than necessary for gain measurements. The amplitude distribution from the LED flash is measured at several values of APD bias voltage in the range from 20 to 395 V. Figure 4 shows the LED amplitude for different voltages for one example channel.

Figure 5 (left) shows the gain-voltage dependence for three channels illustrating the spread of the gains at a given voltage. The APD gain was set to 29 for all channels in order to provide the designed dynamic range of the energy measurement in PHOS. With this requirement, the bias voltage varies from 290 to 395 V, as shown in Fig. 5 (right).

After the equalization of the APD gains, the calibration needs to be further refined to take into account the specific light yield of the different crystals. However, the spread of light yields of the different $PbWO_4$ crystals is relatively small, about 12% [13], and the APD gain equalization can thus be considered as a first step towards the energy calibration based on physics signals from collision events such as the π^0 peak. As a measure of calibration quality, the invariant mass of photon pairs is constructed as follows:

$$m_{\gamma\gamma} = \sqrt{2E_{\gamma,1}E_{\gamma,2}(1-\cos\theta_{12})}, \qquad (2)$$

where $E_{\gamma,i}$ is the energy of the reconstructed photon i, and θ_{12} is the opening angle between the two photons. The invariant mass distribution of cluster pairs detected in PHOS in pp collisions at $\sqrt{s} = 13$

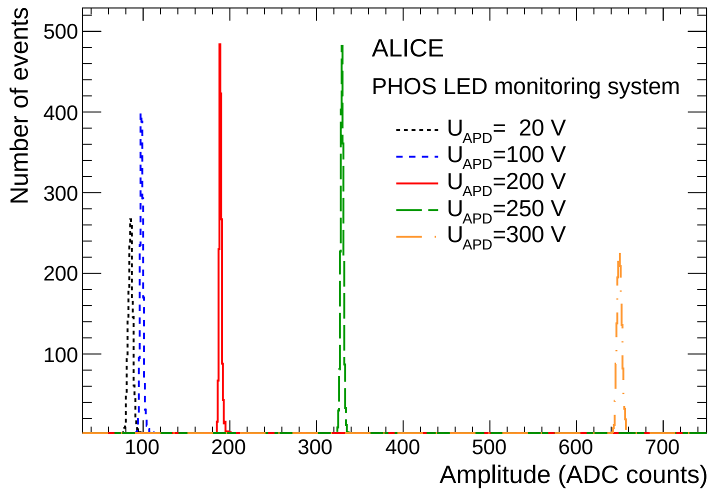

Figure 4: [Color online] Amplitude of LED peak for different APD bias voltages for one example channel.

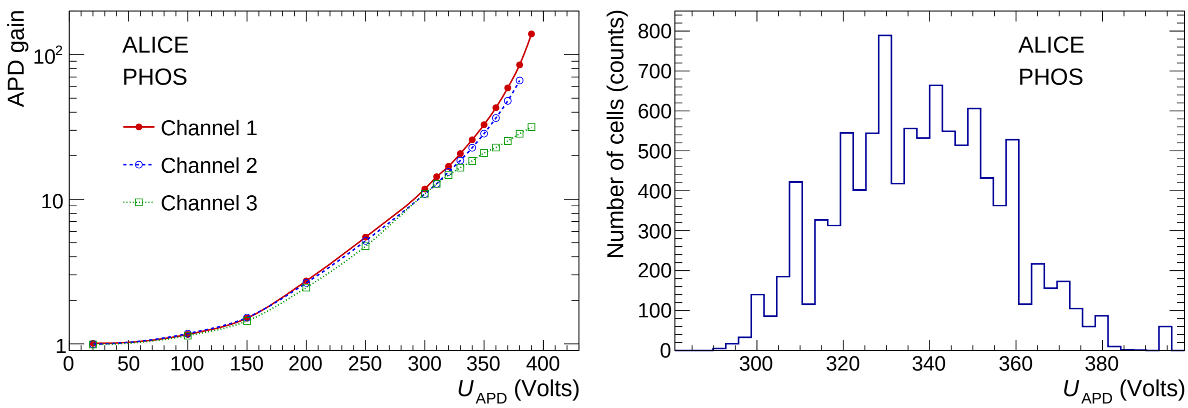

Figure 5: [Color online] Left: Dependence of the APD gain on applied bias voltage for three different channels. Right: Distribution of APD bias voltage for all PHOS cells corresponding to an APD gain of 29.

TeV with a cut on the cluster pair transverse momentum $p_{\mathrm{T}} > 1.7$ GeV$/c$ after APD gain equalization is shown in Fig. 6, where the choice of the low-p_{T} cut is driven by maximizing the signal-to-background ratio and minimizing the energy nonlinearity effects which will be discussed in Section 5. A clear π^0 peak above the combinatorial background is observed. The invariant mass distribution is fitted in the range $35-210$ MeV/c^2 with the sum of a Gaussian and a second order polynomial. The extracted π^0 peak position $\langle m \rangle \approx 113.8 \pm 0.6$ MeV/c^2 is $\sim 15\%$ lower than the PDG value [24] and its width $\sigma_m \approx 13.8 \pm 0.9$ MeV/c^2 is approximately 3 times larger than the expected resolution of 5.5 MeV/c^2 for an ideally calibrated PHOS as described in GEANT-based Monte-Carlo simulations [17]. These values are an acceptable starting point for the final relative PHOS calibration based on π^0 peak equalization described in the following section.

3.3 Calibration using the π^0 peak position

The calibration procedure aims to calculate for each cell i the calibration coefficients α_i relating the energy deposition E_{dep} and the response (measured amplitude) A as $E_{\mathrm{dep}} = \alpha_i \cdot A$. To find them, the di-photon invariant mass distribution is constructed, see Eq. (2). One of the two photons, e.g. γ_1, must hit the cell i under current consideration while the second one, γ_2, is any other photon in the event.

The invariant mass distribution shows a peak corresponding to the π^0 meson at m_i with some mass shift due to miscalibration. The correction to the calibration coefficient, which relates the measured amplitude

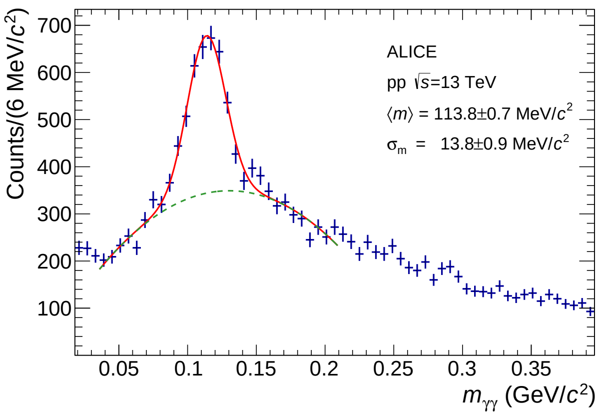

Figure 6: [Color online] Invariant mass distribution of cluster pairs after APD gain equalization in pp collisions at $\sqrt{s} = 13$ TeV for $p_T > 1.7$ GeV/c. The red curve is a fit of the spectrum with the sum of a Gaussian and a second-order polynomial function. The green dashed line is the background contribution only.

A and corrected energy E_{corr} as $E_{corr} = \alpha_i \cdot c_i \cdot A$, is defined by the following equation:

$$c_i = \left(\frac{m_{\pi^0}}{m_i}\right)^n, \quad (3)$$

where m_{π^0} is the true neutral pion mass and $n > 0$ is a parameter that has to be optimized. The procedure is then iteratively applied, with α_i obtained at iteration j being updated to $\alpha_i^{j+1} = \alpha_i^j \cdot c_i$, until no further improvement of a calibration is found. From Eq. (2) and (3) one can expect the best power to be $n = 2$. However, with this choice one implicitly assumes that the influence of calibration of all other cells on average is negligible, which in reality is not the case. To illustrate this, the procedure is applied to a toy model implementing several values of n as described in the next section.

3.3.1 Optimization of the calibration procedure with a toy model

This toy model describes the influence of the simultaneous calibration of different cells of a calorimeter. In a real calorimeter a photon cluster includes a cell with a dominant energy deposition plus a few additional cells. The simplified model assumes that the entire photon energy is deposited in one cell of a calorimeter. In the model, the calorimeter covers a pseudorapidity $|\eta| < 1$ and full azimuthal angle with a granularity of 100×100 cells in the φ and η directions. Each cell has an independent calibration coefficient which initially is randomly assigned according to a Gaussian distribution with mean 1 and a width of 20%.

The particle generator is tuned to produce neutral pions with a flat rapidity and azimuthal distribution and a realistic p_T spectrum as measured in pp collisions at $\sqrt{s} = 7$ TeV [18]. The generated π^0 mesons are forced to decay into photon pairs. The photon energies are smeared according to Eq. (1). A cut on the minimal reconstructed photon energy $E_\gamma > E_{min} = 0.3$ GeV is applied to ensure that energy distributions in the model and data are similar (see section 3.3.2).

Figure 7 shows the dependence of a residual de-calibration σ_c, defined as the RMS of the difference between estimated and true calibration coefficients $\alpha_i - \alpha_i^{true}$ for all cells of the toy simulation, versus iteration number. The value $n \sim 2$ is found to lead to some oscillations and poor convergence of the algorithm. All calibration procedures start from the same initial de-calibration of cells and use the same sample of π^0 mesons. The final precision of the calibration depends on the accuracy of the reconstructed pion peak position for a typical cell, which in turn depends on the peak width (defined by the energy and position resolution) and the available statistics. In the model, the statistics of the simulated pions is defined by a requirement to have 10^3 reconstructed photons per cell after a p_T cut of 1.7 GeV/c on the reconstructed photon pairs, the same as in the calibration using real data as described in section 3.3.2.

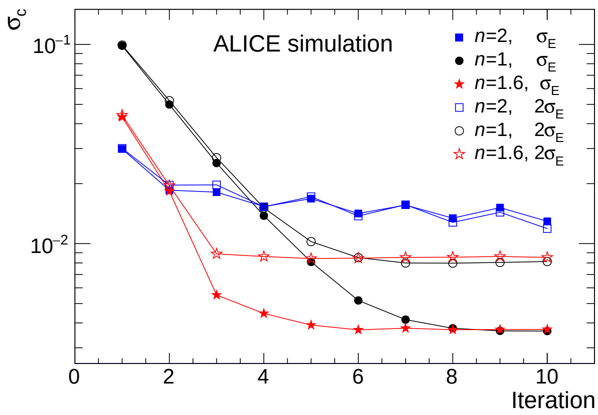

Figure 7: [Color online] Study using a toy Monte-Carlo simulation of the convergence of the iterative calibration procedure based on the equalization of the π^0 peak position. The residual de-calibration σ_c is shown as a function of the iteration number. Two values of calorimeter energy resolution are considered, standard (σ_E) and twice as large ($2\sigma_E$).

To study the dependence of the final calibration accuracy on the energy resolution, the default energy resolution of the toy calorimeter is increased by a factor of 2; these simulations are marked as $2\sigma_{\mathrm{E}}$. For powers $n < 2$, the residual de-calibration saturates at values corresponding to the final precision of the calibration. In the case of $n = 2$, the residual de-calibration rapidly decrease at the first iteration, but after $2-3$ iterations start to fluctuate around a level considerably higher than the saturation of values for $n < 2$.

In order to find the optimal value of n, the RMS of the de-calibration distribution is studied as a function of iteration number for several values of n, see Fig. 8 (left), and versus n for several iterations (right). For large values of n, few iterations are needed to reach saturation. However, better accuracy is obtained for lower values of n. Since each iteration in an analysis with real data is very time-consuming we chose a value of $n = 1.6$ in the next analysis steps, which provides the best accuracy after $2-3$ iterations.

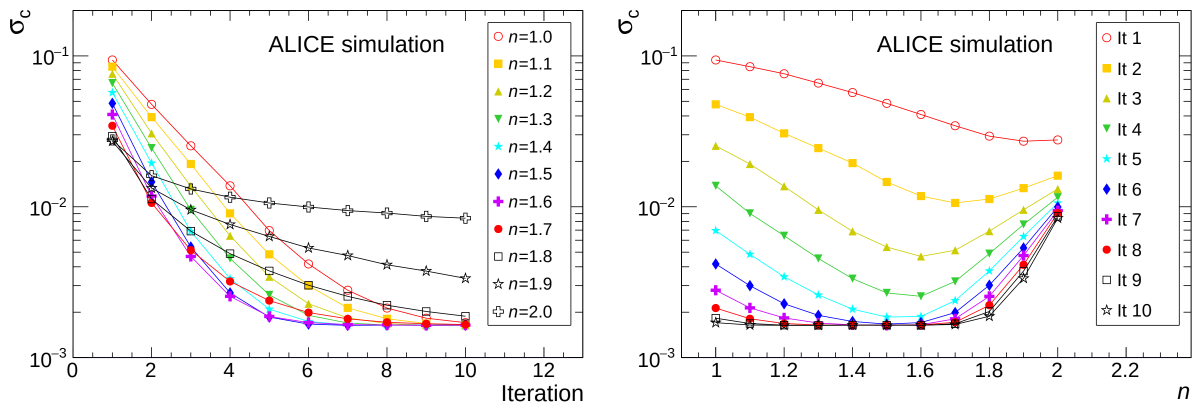

Figure 8: [Color online] Left: Residual de-calibration in the toy model simulation with default energy resolution versus iteration number for several values of power n. Right: Residual de-calibration versus power n for several iterations.

3.3.2 Calibration using pp collision data

The procedure described above is used in the final step of the calibration of the PHOS detector. The calibration is performed using physics data from pp collisions at $\sqrt{s} = 13$ TeV recorded in 2017. The sample contains $7.7 \cdot 10^8$ minimum bias (MB) events and $5 \cdot 10^7$ events recorded with the PHOS L0 trigger [25, 26], corresponding to an integrated luminosity of $\mathscr{L}_{\mathrm{int}} = 12$ nb^{-1} and 5.9 pb^{-1}, respectively.

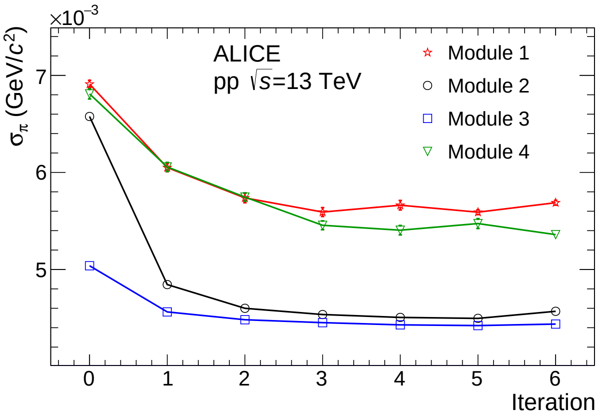

Figure 9: [Color online] Dependence of the π^0 peak width on the iteration number for photon pairs with $p_{\mathrm{T}} > 1.7$ GeV$/c$ in four PHOS modules.

A set of cuts are applied: on the minimum number of cells in a cluster, $N_{\text{cells}} > 2$, the minimum cluster energy $E_{\text{clu}} > E_{\text{min}} = 0.3$ GeV, and the dispersion cut [17]

$$D = \sum w_i((x_i - \bar{x})^2 + (z_i - \bar{z})^2)/w > 0.2\ \text{cm}^2, \tag{4}$$

where x_i, z_i are the coordinates of the cell i, $\bar{x}$, $\bar{z}$ are coordinates of the cluster center of gravity in the PHOS plane and the weights $w = \sum w_i$, with $w_i = \max(0, \log(E_i/E_{\text{clu}}) + 4.5)$ are calculated using the energy deposition in a cell E_i and the total cluster energy E_{clu}. These cuts are used to select photon clusters and reject rare events induced by hadron interactions directly in the APD which result in disproportionally high signals [27]. A minimum pion transverse momentum cut $p_{\mathrm{T}} > 1.7$ GeV$/c$ is imposed to reduce the combinatorial background.

As discussed above, for photon clusters most of the energy ($\sim 80\%$) is deposited in the central cell. Therefore, in our calibration procedure, a calibration correction is only applied to the central cell of a cluster. Clusters which are close to a dead cell are not removed: instead the standard approach is extended to such clusters. As a result, a shower leakage to bad cells is compensated by higher calibration coefficients in adjacent good cells. At each iteration the correction for the calibration coefficients is calculated using power $n = 1.6$. Figure 9 shows that about 3 iterations are sufficient to reach an almost final calibration. This is in good agreement with the predictions of the toy Monte Carlo. The width of the peak in modules 2 and 3 is close to what is expected from Monte-Carlo simulations by taking into account the $PbWO_4$ response and ideal calibration. In modules 1 and 4, the width is larger because of a batch of front-end electronics cards with somewhat higher noise characteristics.

4 Check of the energy scale

Fixing the π^0 peak position to the PDG value does not mean fixing the absolute energy scale of the calorimeter. As shown in Eq. (2), the measured mass depends both on the cluster energy and on the opening angle. If the description of the detector geometry in the reconstruction software differs from reality, some bias is introduced into the absolute energy scale. To check this one needs some independent methods. In our case the cross-check was performed with the electron E/p ratio using identified electrons from the ALICE central tracking system consisting of the Inner Tracking System (the ITS) [28] and Time Projection Chamber (the TPC) [29] (see section 4.1) and by matching tracks with PHOS clusters (see section 4.2).

4.1 Calibration using identified electrons

Using electrons for the absolute energy calibration of an electromagnetic calorimeters is a widely used approach [10]. Electrons, like photons, deposit their total energy in the calorimeter and it is possible to compare the energy measured in the calorimeter with the momentum of an electron reconstructed in the tracking system upstream of the calorimeter. There are two advantages of this approach compared to the calibration using the π^0 mass peak: first, one considers single clusters and no iterative procedure is necessary; second, it does not depend on the exact position of the calorimeter and its geometrical mis-alignment, appearing in the calculation of the opening angle θ_{12} in the Eq. (2), is not mixed with energy calibration. Disadvantages of this method are the limited number of reconstructed electrons and the strong sensitivity to the material budget in front of the calorimeter. There are no such drawbacks in a beam-test calibration using electrons, which is usually performed before installation of a calorimeter. Furthermore, this method can be used as a cross-check for the calibration using the π^0 mass peak.

The same data sample is used for the calibration via electrons in real data as for the calibration using the π^0 mass peak, namely pp collisions at $\sqrt{s} = 13$ TeV. Charged tracks are reconstructed with the ALICE central tracking system. In the calorimeter, electrons can be independently identified by investigating the ratio E/p, where E is the energy of a cluster in the calorimeter and p is the momentum of a track, reconstructed by the tracking system, see Fig. 10. However, in this analysis the E/p peak is not used for the electron identification but for the calibration of the calorimeter. One can reduce the background both at low and high p_{T} and keep the efficiency close to 100% by selecting clusters corresponding to the electromagnetic shower transverse size (marked as 'EM clusters' in Fig. 10) applying cuts on cluster dispersion, defined in Eq. (4). To improve the accuracy of the peak position extraction, the signal-to-background ratio is further increased by taking electrons identified via the specific ionization energy loss dE/dx in the TPC [29, 30]. This method is efficient at low p_{T}, while at the region of the relativistic rise for pions $p_{\mathrm{T}} \gtrsim 1$ GeV$/c$ a separation of pions and electrons becomes increasingly difficult. The available statistics is not sufficient to perform a channel-by-channel calibration for all 12 544 channels with good accuracy.

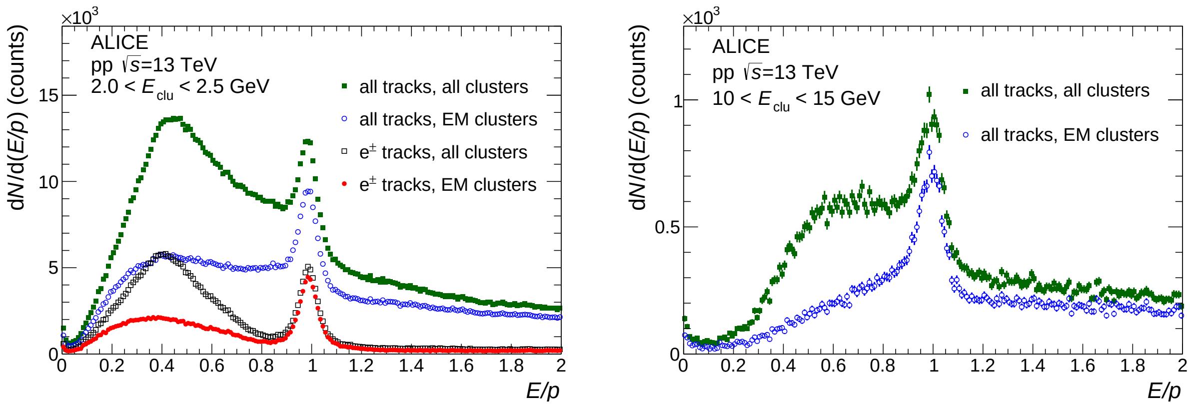

Figure 10: [Color online] Distribution of the cluster energy to track momentum, E/p ratio, for two ranges of cluster energies E_{clu} in one PHOS module. A peak around unity due to the electron contribution is visible.

Fitting the E/p distributions, the peak position and the peak width are extracted as a function of cluster energy in two middle PHOS modules with the best energy resolution, see Fig. 11. At high p_{T}, the mean is close to unity, but gradually decreases towards smaller p_{T}, reflecting an increased relative energy loss of lower energy electrons. In the same figure the measured E/p peak position and width are compared with the same quantities calculated with Monte-Carlo simulations of pp collisions with the PYTHIA8 event generator [31] and reconstructed with the standard ALICE software framework used for real data. The simulation includes a remaining small mis-calibration describing an inaccuracy of our calibration to reproduce the π^0 mass peak position and width and their dependence on p_{T}. The agreement is better than $\sim 0.2\%$ providing an independent estimate of the absolute energy scale uncertainty in PHOS.

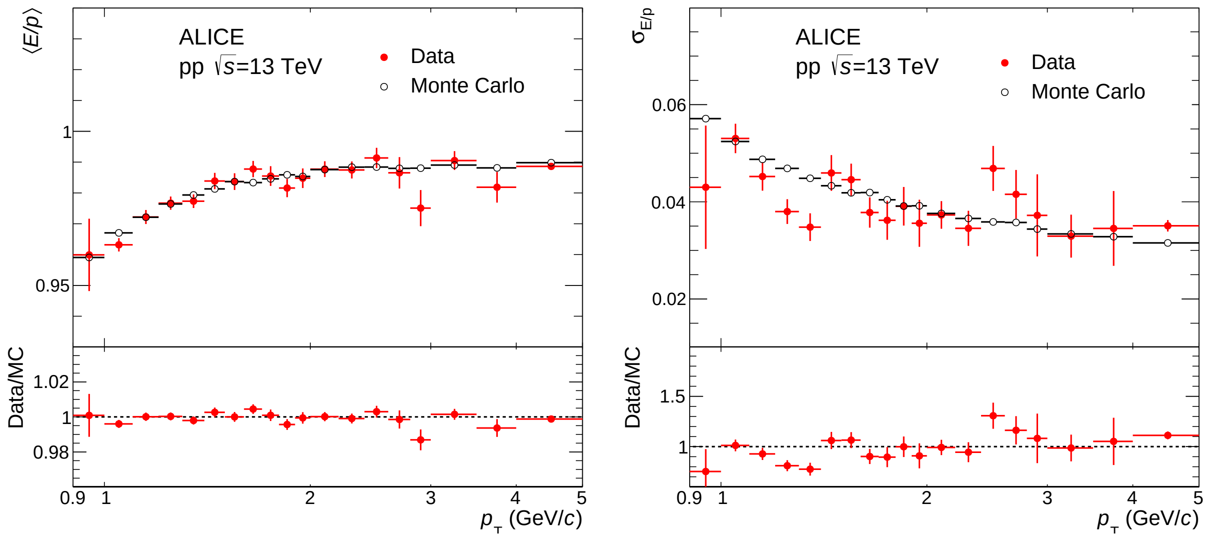

Figure 11: [Color online] Mean (left) and width (right) of the E/p peak position in data and MC for electron candidates.

4.2 Geometrical alignment

The two-photon invariant mass, defined in Eq. (2), can also be expressed as

$$m_{\gamma\gamma} = 2\sqrt{E_1E_2}|\sin(\theta_{12}/2)| \approx \sqrt{E_1E_2}\frac{L_{12}}{R}, \tag{5}$$

where L_{12} is the distance between clusters in a calorimeter and R is the distance from the interaction point (IP) to the calorimeter. Uncertainties in the measurement of R directly translate to uncertainties in the energy scale. The precise measurement of the distance between the IP and the calorimeter surface is a difficult task because of the inner detectors installed in a typical collider experiment. The alignment of the PHOS was measured via the photogrammetry procedure [32] but in addition, an independent estimate of the PHOS alignment is performed by matching tracks reconstructed in the tracking system with clusters in PHOS. To study the alignment it is convenient to use the local coordinate system of the PHOS module where z is the coordinate along the beam and x is the coordinate perpendicular to the beam direction. The alignment in z and x directions is straightforward, while checking the most important misalignment in the radial direction is more complicated.

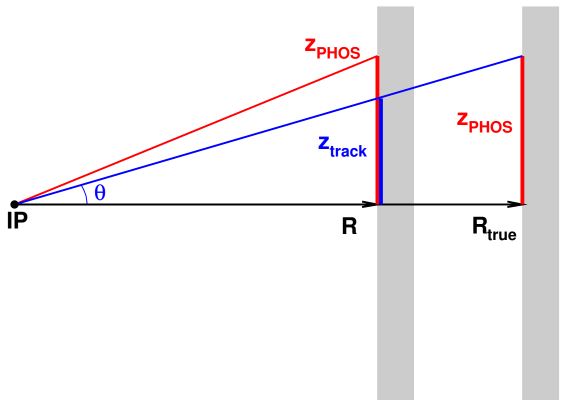

Figure 12: [Color online] Illustration of the dependence of $\langle dz \rangle$ on z in a radially shifted detector.

One can express the difference between the z coordinate of the reconstructed cluster position in the calorimeter, z_{PHOS}, and the point of the track extrapolated to the surface of the calorimeter, z_{track}, through the ratio of true (R_{true}) and expected (R) radial distances (see Fig. 12 for the variable definition):

$$dz = z_{\mathrm{PHOS}} - z_{\mathrm{track}} = z_{\mathrm{PHOS}} - R\tan\theta = z_{\mathrm{PHOS}}\left(1 - \frac{R}{R_{\mathrm{true}}}\right). \quad (6)$$

In this procedure it is assumed that the depth of the maximal energy deposition of a shower corresponds to the one of a photon [17] and a correction for this depth is introduced to the cluster center of gravity so that x and z coordinates correspond to those of the photon which crossed the front surface of PHOS. In contrast to photons and electrons, because of the large nuclear interaction length of the EM calorimeter, the center of gravity of a hadronic shower is almost uniformly distributed in the depth of the calorimeter and therefore hadronic tracks are not suitable for such calibration. Electron showers are very similar to the ones of photons but reach their maximum about one unit in radiation length X_0 earlier than photons. Therefore, the correction term to account for the difference between default (photon) and electron z coordinate of the cluster due to the different depths of their showers can be written as

$$\delta z_{\mathrm{e}} = -X_0 \sin\left(\arctan\frac{z_{\mathrm{PHOS}}}{R_{\mathrm{true}}}\right). \quad (7)$$

This effect corresponds to the slope $B_{\mathrm{e}} = -0.19\cdot 10^{-2}$ in the dependence of mean difference $\langle dz\rangle$ versus z distribution. Figure 13 shows the mean $\langle dz\rangle$ versus z distribution, and analogously, the $\langle dx\rangle(x)$ dependence. For the latter observable, the measured $\langle dx\rangle$ values for electrons and positrons are separately shown. In case of the $\langle dz\rangle(z)$ study, the distributions in the two modules are very close to each other and show a similar slope. There are some oscillations around the linear dependence. The extracted slope, shown in the plot for both modules, is slightly larger than B_{e}, which one could expect for an ideally aligned detector. The difference corresponds to ~ 4 mm inward radial shift of the PHOS modules. These values were used to correct the radial PHOS position in the offline reconstruction. The $\langle dx\rangle(x)$ distributions for positive and negative charges have similar slopes but opposite offsets because of the track bending in the magnetic field, which results in different incident angles for electrons and positrons with respect to photons. The extracted cluster coordinates should be corrected for the difference in incident angles, which strongly depends on the particle p_{T}, making this analysis much more complicated compared to the $\langle dz\rangle(z)$ study. Therefore, only the latter is used in the PHOS alignment procedure.

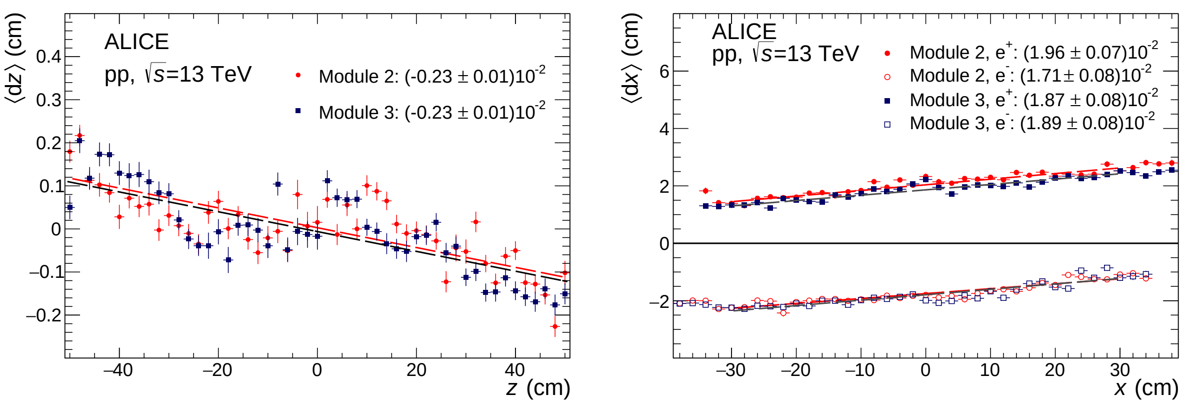

Figure 13: [Color online] Dependence of the mean distance between track extrapolation to the PHOS surface and cluster position in the cluster coordinate on the PHOS plane along (left) and perpendicular (right), to the beam direction. In the left plot contributions of electrons and positrons are combined. The dependencies are fitted with linear functions and the resulting slopes are shown in the legend.

5 Estimate of the energy nonlinearity correction

There are several effects which may influence the linearity of PHOS energy measurement: light attenuation in crystals, electronic noise, electronic threshold and amplitude digitization are important mostly at low energies, while shower leakage contributes to a nonlinear response at high energies. For the physics analysis it is sufficient to reproduce the observed nonlinearity of the detector in the Monte-Carlo simulations, but practically, it is more convenient to correct real data for the nonlinearity in order to reduce the mass resolution of a neutral meson peak in wide p_{T} bins.

The nonlinearity is corrected via recalculation of the cluster energy E by the following parameterization:

$$E_{\mathrm{corr}} = \begin{cases} aE + b\sqrt{E} + c + d/\sqrt{E} + e/E, & E \leq E_0 \\ \alpha E + \beta\sqrt{E}, & E > E_0 \end{cases} \tag{8}$$

where free parameters a, b, c, d, e, E_0 are chosen to provide a p_{T}-independent reconstructed neutral pion mass m_{π^0} in pp collisions at $\sqrt{s} = 13$ TeV and parameters α and β are fixed to ensure a smooth function at the point $E = E_0$.

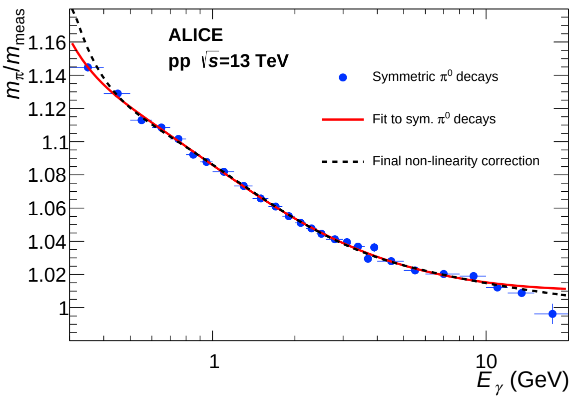

Figure 14: [Color online] Estimation of PHOS nonlinearity using symmetric π^0 decays with asymmetry $|E_{\gamma,1} - E_{\gamma,2}| < 0.05(E_{\gamma,1} + E_{\gamma,2})$. Data fit with function (8). Final tuned nonlinearity is shown with a dashed curve.

The initial seed for the parameter tuning procedure is obtained by fitting the ratio of the PDG π^0 mass to the measured π^0 peak position for symmetric decays $|E_{\gamma,1} - E_{\gamma,2}| < 0.05(E_{\gamma,1} + E_{\gamma,2})$, as a function of mean photon energy E_γ, see Fig. 14. The fit with the function $E_{\mathrm{corr}}(E)/E$ (eq.8) is shown by a red curve in Fig. 14. However, this method is not reliable at very low energies where, because of limited PHOS acceptance, the systematic uncertainties of the π^0 signal extraction are high, and at high p_{T} where photons from symmetric decays start to merge into one cluster. To improve the nonlinearity parameterization, a set of invariant mass distributions was calculated without asymmetry selection, each of them were corrected for nonlinearity with different sets of nonlinearity parameters (a, b, c, d, e, E_0). A few examples of the dependencies of peak position on p_{T} are shown in Fig. 15 (left). Depending on the set of parameters (b, c, d, e), the peak position shows some p_{T} dependence. Note that parameter a reflects absolute normalization and can be factorized in this analysis. To find the best set of parameters, a fit of the peak p_{T}-dependence with a constant function is performed in the range $0.6 - 25$ GeV$/c$. The resulting χ^2 value for each set of parameters is shown in Fig. 15 (right). In this plot we fix optimal values of parameters a, b, c, E_0 and vary only parameters d, e. The optimal set, obtained by minimizing χ^2, is ($a = 1.02 \pm 0.01$, $b = -0.2548 \pm 0.0005$ GeV$^{1/2}$, $c = 0.648 \pm 0.001$ GeV, $d = -0.4743 \pm 0.0002$ GeV$^{3/2}$, $e = 0.1215 \pm 0.0005$ GeV^2 and $E_0 = 5.17 \pm 0.01$ GeV). Nonlinearity correction corresponding to this set is shown with a black dashed line in Fig. 14. This parameter set, corresponding to the filled red circles in the left plot of Fig. 15, is used in the offline reconstruction.

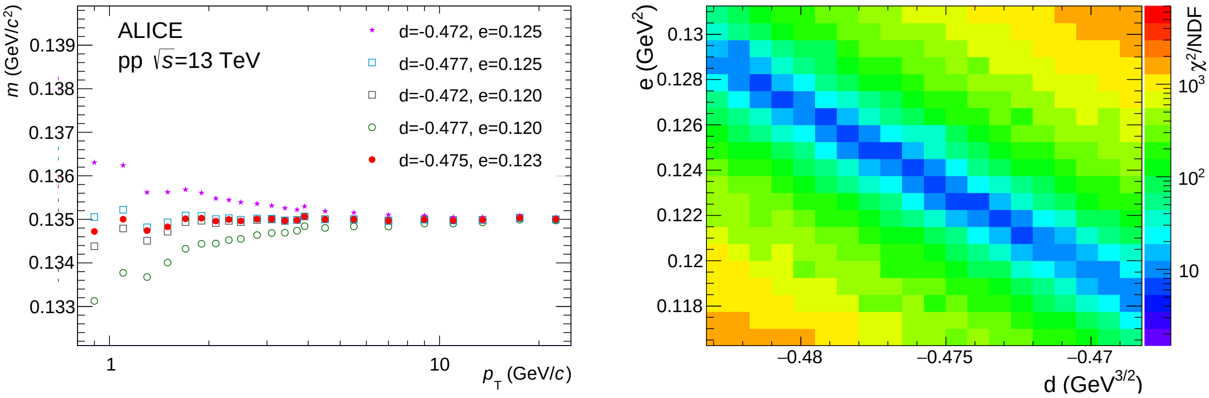

Figure 15: [Color online] Left: the π^0 peak position as a function of the transverse momentum for several values of nonlinearity parameters (d, e) and default values for others. Right: the deviation from a constant value of the π^0 peak position expressed in χ^2/NDF as a function of nonlinearity parameters (d, e).

6 Run-by-run energy calibration

Both scintillating crystals $PbWO_4$ and APDs have a strongly temperature dependent light yield and amplification, respectively. To minimize this effect on the PHOS energy scale, the PHOS crystal matrices were thermo-stabilized at an accuracy better than 0.3°C. This temperature variation results in change of about 0.6% in light yield and APD gain. Another effect which may influence the long-term stability of the amplitude measurement in the PHOS detector is the crystal transparency dependence on the radiation dose. A run-dependent calibration correction common for all channels in each PHOS module was implemented to account for all these effects. In order to estimate this correction, all previously described calibrations and corrections were applied, and for each run the mean value of the π^0 mass peak, reconstructed only of photon pairs detected in the same module, was extracted.

The correction is calculated using the data sample collected with the PHOS L0 trigger since it has better statistics at high p_T, where the signal-to-background ratio is larger. The evolution of the correction is illustrated using 400 subsequent runs of pp collisions at $\sqrt{s} = 13$ TeV recorded during 3 months of data taking from June to September 2017 with stable running conditions. The trend plots of the reconstructed π^0 mass peak position versus consecutive run index is illustrated in Fig. 16 for two middle PHOS modules with the largest acceptance and the best energy resolution. On average the peak position is stable within ~ 2 MeV/c^2 in both modules, but reveals several correlated and uncorrelated trends in these two modules. Correlated trends are related to the powering of the PHOS front-end electronics in both modules, and therefore to the variation of the heat deposition and temperature of the crystal matrix. Uncorrelated trends may have different reasons: switching on or off isolated front-end cards, formation of ice jams in the cooling pipes of the cooling system, etc. There is no visible global correlated trend of a decrease of the peak position in all modules, which would indicate a radiation damage in the crystals and a decrease of their transparency with time.

In the calibration procedure the mean value of the peak position over the whole period is calculated and deviations with respect to this value are estimated. If the peak position in a module is known with uncertainty better than 1 MeV, all calibration coefficients in a module are corrected by the ratio $m_{\rm mean}/m_{\rm run}$. If a run is too short and fitting is not possible, the mean value is used.

7 Results of calibration

The invariant mass spectrum of cluster pairs after applying all calibration corrections is shown in Fig. 17 in the region of π^0 (left) and η-meson (right) peaks. All four PHOS modules were considered. It reveals a much narrower π^0 peak and better signal-to-background ratio compared to the pre-calibrated result

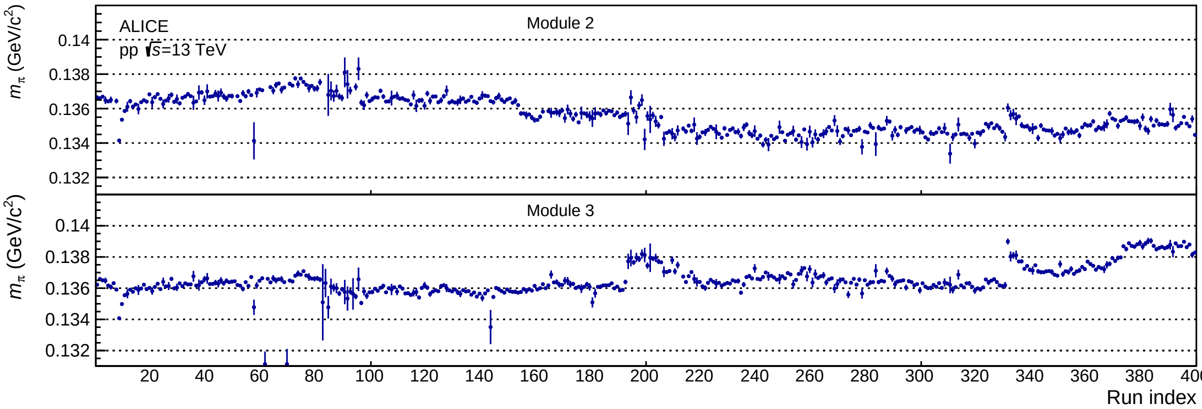

Figure 16: [Color online] Example of the dependence of the π^0 peak position on the run number for 400 subsequent runs recorded during 3 months of the 2017 data taking campaign.

shown in Fig. 6. The improved calibration allows to resolve details of the shape of π^0 peak, therefore mass distribution is fitted with a sum of a Crystal Ball function [33] for the peak description and a polynomial of the second order for the combinatorial background. For the η meson a sum of Gaussian and second order polynomial is used. Both the π^0 and η meson peak positions are consistent with their PDG values $m_{\pi^0} = 134.98$ MeV$/c^2$ and $m_\eta = 547.9$ MeV$/c^2$ within statistical uncertainties, as illustrated in Fig. 17. The agreement of the η peak position with the PDG values provides a cross-check of the correctness of the description of the PHOS alignment in the ALICE setup and therefore, of the absolute energy calibration.

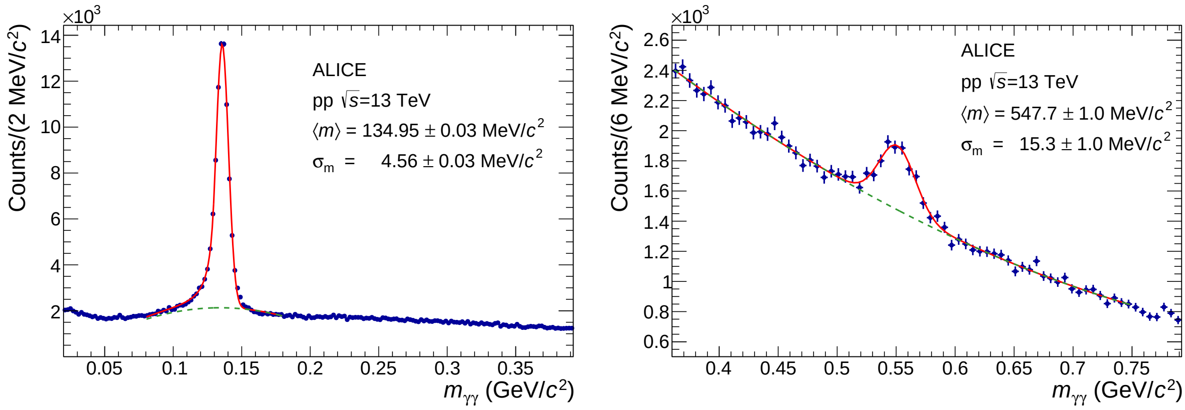

Figure 17: [Color online] Invariant mass distributions of cluster pairs for $p_{\mathrm{T}} > 1.7$ GeV$/c$ in the π^0 (left) and η (right) mass region after calibration with per-channel π^0 peak equalization. Solid curves show the fitting function defined as a sum of the Crystal Ball and polynomial functions and dashed lines represent the background contribution.

Finally, the peak positions and peak widths of the π^0 and η mesons are measured in the bins of transverse momentum, see Fig. 18. The width of the π^0 peak reaches a minimum value $\sigma \approx 4$ MeV$/c^2$ at $p_{\mathrm{T}} = 3-8$ GeV$/c$. The reconstructed mass remains approximately constant up to $p_{\mathrm{T}} \sim 25$ GeV$/c$, and increases with p_{T} afterwards. This is a reflection of the fact that starting from this p_{T} region, a considerable fraction of cluster pairs from daughter photons start to overlap and the reconstruction software has a bias towards clusters that are better separated due to fluctuations in the energy deposition, thus increasing the extracted pion mass. In the case of the η meson, the peak position is stable since the influence of the overlap in this case should appear from $p_{\mathrm{T}} \sim 80$ GeV$/c$.

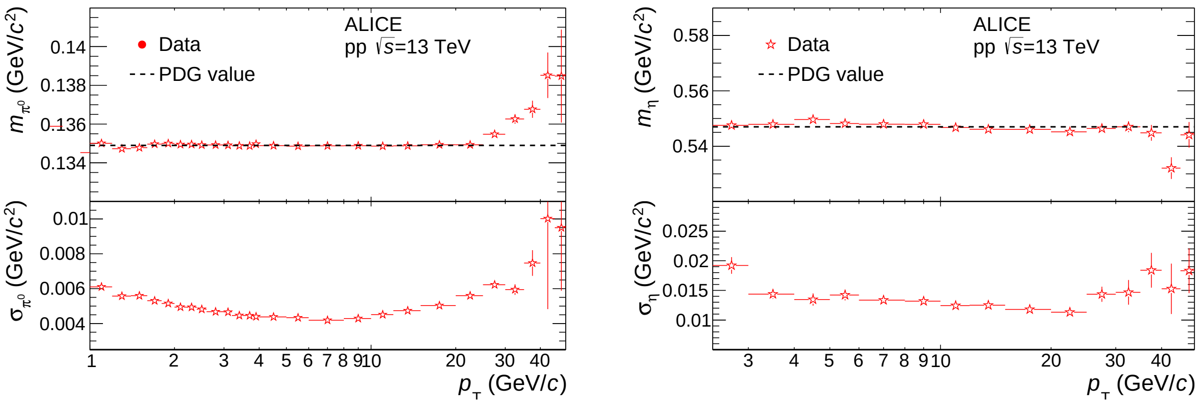

Figure 18: [Color online] Peak position and width for π^0 (left) and η mesons (right) as a function of transverse momentum. Vertical error bars represent fit uncertainties.

8 Conclusions

In this paper all steps of the calibration of the ALICE electromagnetic calorimeter PHOS from a completely uncalibrated state to the set of calibration parameters which ensure a performance equivalent to Monte-Carlo simulations with an ideally calibrated detector are presented. Pre-calibration with equalization of the photodetector gains is provided by the use of the monitoring system with light-emitting diodes. This preliminary calibration serves as a starting point for the energy calibration based on adjusting the reconstructed π^0 mass from data collected in high-luminosity proton-proton collisions. The calibration coefficients averaged over a large period of data taking are obtained with this relative calibration procedure. The absolute energy scale is verified by analyzing pp data with electron tracks reconstructed in the ALICE central tracking system and matched with PHOS clusters. An accurate correction of the PHOS geometrical alignment in the radial direction, also achieved using electron tracks, is necessary for the absolute energy calibration. Further refining of the calibration is performed by correcting the PHOS response for energy nonlinearity effects. Finally, the calibration is corrected for time variations in performance due to changes in running conditions and power dissipation in the front-end electronics of the detector. The resulting time-dependent calibration parameters of the PHOS spectrometer ensure stable response and the best possible resolution of the detector over a large time span. After applying all calibration steps in the reconstruction of pp collision data at $\sqrt{s} = 13$ TeV, π^0 and η meson peak positions close to their PDG mass values over a wide p_T range are obtained and the achieved mass resolution is $\sigma_m^{\pi^0} = 4.56 \pm 0.03$ MeV/c^2 and $\sigma_m^{\eta} = 15.3 \pm 1.0$ MeV/c^2 (for $p_T > 1.7$ GeV/c).

Acknowledgements

The ALICE Collaboration would like to thank all its engineers and technicians for their invaluable contributions to the construction of the experiment and the CERN accelerator teams for the outstanding performance of the LHC complex. The ALICE Collaboration gratefully acknowledges the resources and support provided by all Grid centres and the Worldwide LHC Computing Grid (WLCG) collaboration. The ALICE Collaboration acknowledges the following funding agencies for their support in building and running the ALICE detector: A. I. Alikhanyan National Science Laboratory (Yerevan Physics Institute) Foundation (ANSL), State Committee of Science and World Federation of Scientists (WFS), Armenia; Austrian Academy of Sciences, Austrian Science Fund {FWF}: [M 2467-N36] and Nationalstiftung für Forschung, Technologie und Entwicklung, Austria; Ministry of Communications and High Technologies, National Nuclear Research Center, Azerbaijan; Conselho Nacional de Desenvolvimento Científico e Tecnológico (CNPq), Universidade Federal do Rio Grande do Sul (UFRGS), Financiadora de Estudos e Projetos (Finep) and Fundação de Amparo à Pesquisa do Estado de São Paulo (FAPESP), Brazil; Ministry of Science & Technology of China (MSTC), National Natural Science Foundation of China (NSFC) and Ministry of Education of China (MOEC) , China; Croatian Science Foundation and Ministry of Science and Education, Croatia; Centro de Aplicaciones Tecnológicas y Desarrollo Nuclear (CEADEN), Cubaenergía, Cuba; Ministry of Education, Youth and Sports of the Czech Republic, Czech Republic; The Danish Council for Independent Research — Natural Sciences, the Carlsberg Foundation and Danish National Research Foundation (DNRF), Denmark; Helsinki Institute of Physics (HIP), Finland; Commissariat à l'Energie Atomique (CEA), Institut National de Physique Nucléaire et de Physique des Particules (IN2P3) and Centre National de la Recherche Scientifique (CNRS) and Rlégion des Pays de la Loire, France; Bundesministerium für Bildung, Wissenschaft, Forschung und Technologie (BMBF) and GSI Helmholtzzentrum für Schwerionenforschung GmbH, Germany; General Secretariat for Research and Technology, Ministry of Education, Research and Religions, Greece; National Research, Development and Innovation Office, Hungary; Department of Atomic Energy Government of India (DAE), Department of Science and Technology, Government of India (DST), University Grants Commission, Government of India (UGC) and Council of Scientific and Industrial Research (CSIR), India; Indonesian Institute of Science, Indonesia; Centro Fermi - Museo Storico della Fisica e Centro Studi e Ricerche Enrico Fermi and Istituto Nazionale di Fisica Nucleare (INFN), Italy; Institute for Innovative Science and Technology , Nagasaki Institute of Applied Science (IIST), Japan Society for the Promotion of Science (JSPS) KAKENHI and Japanese Ministry of Education, Culture, Sports, Science and Technology (MEXT), Japan; Consejo Nacional de Ciencia (CONACYT) y Tecnología, through Fondo de Cooperación Internacional en Ciencia y Tecnología (FONCICYT) and Dirección General de Asuntos del Personal Academico (DGAPA), Mexico; Nederlandse Organisatie voor Wetenschappelijk Onderzoek (NWO), Netherlands; The Research Council of Norway, Norway; Commission on Science and Technology for Sustainable Development in the South (COMSATS), Pakistan; Pontificia Universidad Católica del Perú, Peru; Ministry of Science and Higher Education and National Science Centre, Poland; Korea Institute of Science and Technology Information and National Research Foundation of Korea (NRF), Republic of Korea; Ministry of Education and Scientific Research, Institute of Atomic Physics and Ministry of Research and Innovation and Institute of Atomic Physics, Romania; Joint Institute for Nuclear Research (JINR), Ministry of Education and Science of the Russian Federation, National Research Centre Kurchatov Institute, Russian Science Foundation and Russian Foundation for Basic Research, Russia; Ministry of Education, Science, Research and Sport of the Slovak Republic, Slovakia; National Research Foundation of South Africa, South Africa; Swedish Research Council (VR) and Knut & Alice Wallenberg Foundation (KAW), Sweden; European Organization for Nuclear Research, Switzerland; National Science and Technology Development Agency (NSDTA), Suranaree University of Technology (SUT) and Office of the Higher Education Commission under NRU project of Thailand, Thailand; Turkish Atomic Energy Agency (TAEK), Turkey; National Academy of Sciences of Ukraine, Ukraine; Science and Technology Facilities Council (STFC), United Kingdom; National Science Foundation of the United States of America (NSF) and United States Department of Energy, Office of Nuclear Physics (DOE NP), United States of America.

References

[1] **ALICE** Collaboration, K. Aamodt *et al.*, "The ALICE experiment at the CERN LHC," *JINST* **3** (2008) S08002.

[2] **ALICE** Collaboration, G. Dellacasa *et al.*, "ALICE technical design report of the photon spectrometer (PHOS)," CERN-LHCC-99-04.

[3] **ALICE** Collaboration, P. Cortese *et al.*, "ALICE electromagnetic calorimeter technical design report," CERN-LHCC-2008-014, CERN-ALICE-TDR-014.

[4] J. Allen *et al.*, "ALICE DCal: An Addendum to the EMCal Technical Design Report Di-Jet and

Hadron-Jet correlation measurements in ALICE," CERN-LHCC-2010-011, ALICE-TDR-14-add-1.

[5] **LHCb** Collaboration, "LHCb calorimeters: Technical design report," CERN-LHCC-2000-036.

[6] D. Pereima, "Calibration of the LHCb calorimetric system," *JINST* **12** no. 06, (2017) C06016.

[7] **LHCb** Collaboration, I. Belyaev, D. Savrina, R. Graciani, and A. Puig, "Kali: The framework for fine calibration of the LHCb electromagnetic calorimeter," *J. Phys. Conf. Ser.* **331** (2011) 032050.

[8] **CMS** Collaboration, "CMS: The electromagnetic calorimeter. Technical design report," CERN-LHCC-97-33, CMS-TDR-4.

[9] **CMS** Collaboration, G. Fasanella, "High precision, low disturbance calibration system for the CMS Barrel Electromagnetic Calorimeter High Voltage apparatus," *JINST* **12** no. 01, (2017) C01090.

[10] **CMS** Collaboration, S. Chatrchyan *et al.*, "Energy Calibration and Resolution of the CMS Electromagnetic Calorimeter in *pp* Collisions at $\sqrt{s} = 7$ TeV," *JINST* **8** (2013) P09009, `arXiv:1306.2016 [hep-ex]`. [JINST8,9009(2013)].

[11] **ATLAS** Collaboration, "ATLAS liquid argon calorimeter: Technical design report," CERN-LHCC-96-41.

[12] **ATLAS** Collaboration, G. Aad *et al.*, "Electron and photon energy calibration with the ATLAS detector using LHC Run 1 data," *Eur. Phys. J.* **C74** no. 10, (2014) 3071, `arXiv:1407.5063 [hep-ex]`.

[13] M. Ippolitov *et al.*, "Lead tungstate crystals for the ALICE/CERN experiment," *Nucl. Instrum. Meth.* **A537** (2005) 353–356.

[14] K. A. Balygin *et al. Instrum. Exp. Tech.* **61** no. 5, (2018) 639–644.

[15] M. Yu. Bogolyubsky, D. I. Patalakha, V. S. Petrov, B. V. Polishchuk, A. S. Solovev, S. A. Sadovsky, V. A. Senko, and Yu. V. Kharlov, "A light-emitting diode monitoring system of the PHOS photon spectrometer in the ALICE experiment on the Large Hadron Collider," *Instrum. Exp. Tech.* **55** (2012) 11–21. [Prib. Tekh. Eksp.2012,no.1,16(2012)].

[16] **ALICE** Collaboration, P. Cortese *et al.*, "Technical Design Report of the Trigger Data Acquisition High-Level Trigger and Control System," CERN-LHCC-2003-062, CERN-ALICE-TDR-010.

[17] **ALICE** Collaboration, C. W. Fabjan *et al.*, "ALICE: Physics performance report, volume II," *J. Phys.* **G32** (2006) 1295–2040.

[18] **ALICE** Collaboration, B. Abelev *et al.*, "Neutral pion and η meson production in proton-proton collisions at $\sqrt{s} = 0.9$ TeV and $\sqrt{s} = 7$ TeV," *Phys. Lett.* **B717** (2012) 162–172, `arXiv:1205.5724 [hep-ex]`.

[19] **ALICE** Collaboration, B. B. Abelev *et al.*, "Neutral pion production at midrapidity in pp and Pb-Pb collisions at $\sqrt{s_{\rm NN}} = 2.76$TeV," *Eur. Phys. J.* **C74** no. 10, (2014) 3108, `arXiv:1405.3794 [nucl-ex]`.

[20] **ALICE** Collaboration, S. Acharya *et al.*, "π^0 and η meson production in proton-proton collisions at $\sqrt{s} = 8$ TeV," *Eur. Phys. J.* **C78** no. 3, (2018) 263, `arXiv:1708.08745 [hep-ex]`.

[21] **ALICE** Collaboration, S. Acharya *et al.*, "Neutral pion and η meson production in p-Pb collisions at $\sqrt{s_{\rm NN}} = 5.02$ TeV," *Eur. Phys. J.* **C78** no. 8, (2018) 624, `arXiv:1801.07051 [nucl-ex]`.

[22] **ALICE** Collaboration, J. Adam *et al.*, "Direct photon production in Pb-Pb collisions at $\sqrt{s_{\rm NN}}$ = 2.76 TeV," *Phys. Lett.* **B754** (2016) 235–248, `arXiv:1509.07324 [nucl-ex]`.

[23] **ALICE** Collaboration, S. Acharya *et al.*, "Direct photon elliptic flow in Pb-Pb collisions at $\sqrt{s_{\rm NN}}$ = 2.76 TeV," *Phys. Lett.* **B789** (2019) 308–322, `arXiv:1805.04403 [nucl-ex]`.

[24] **Particle Data Group** Collaboration, M. Tanabashi *et al.*, "Review of Particle Physics," *Phys. Rev.* **D98** no. 3, (2018) 030001.

[25] D. Wang *et al.*, "Level-0 trigger algorithms for the ALICE PHOS detector," *Nucl. Instrum. Meth.* **A629** (2011) 80–86.

[26] J. Kral, T. Awes, H. Muller, J. Rak, and J. Schambach, "L0 trigger for the EMCal detector of the ALICE experiment," *Nucl. Instrum. Meth.* **A693** (2012) 261–267.

[27] W. Bialas and D. A. Petyt, "Mitigation of anomalous APD signals in the CMS ECAL," *JINST* **8** (2013) C03020.

[28] **ALICE** Collaboration, G. Dellacasa *et al.*, "ALICE technical design report of the inner tracking system (ITS)," CERN-LHCC-99-12.

[29] J. Alme *et al.*, "The ALICE TPC, a large 3-dimensional tracking device with fast readout for ultra-high multiplicity events," *Nucl. Instrum. Meth.* **A622** (2010) 316–367, `arXiv:1001.1950 [physics.ins-det]`.

[30] **ALICE** Collaboration, J. Adam *et al.*, "Measurement of electrons from heavy-flavour hadron decays in p-Pb collisions at $\sqrt{s_{\rm NN}}$ = 5.02 TeV," *Phys. Lett.* **B754** (2016) 81–93, `arXiv:1509.07491 [nucl-ex]`.

[31] T. Sjstrand, S. Ask, J. R. Christiansen, R. Corke, N. Desai, P. Ilten, S. Mrenna, S. Prestel, C. O. Rasmussen, and P. Z. Skands, "An Introduction to PYTHIA 8.2," *Comput. Phys. Commun.* **191** (2015) 159–177, `arXiv:1410.3012 [hep-ph]`.

[32] R. Goudard, C. Lasseur, and D. Mergelkuhl, "Digital Photogrammetry Applied to Large Physics Detectors," In: Proc. FIG working week, 13–17 April 2003, Paris, France. `https://www.fig.net/resources/proceedings/fig_proceedings/fig_2003/`.

[33] M. J. Oreglia, *"A Study of the Reactions $\psi' \to \gamma\gamma\psi$".* PhD thesis, SLAC, Stanford University, Stanford, California 94305, 1980. `http://www.slac.stanford.edu/pubs/slacreports/slac-r-236.html`.

A The ALICE Collaboration

S. Acharya[140] , F.T.-. Acosta[20] , D. Adamová[93] , S.P. Adhya[140] , A. Adler[74] , J. Adolfsson[80] , M.M. Aggarwal[98] , G. Aglieri Rinella[34] , M. Agnello[31] , Z. Ahammed[140] , S. Ahmad[17] , S.U. Ahn[76] , S. Aiola[145] , A. Akindinov[64] , M. Al-Turany[104] , S.N. Alam[140] , D.S.D. Albuquerque[121] , D. Aleksandrov[87] , B. Alessandro[58] , H.M. Alfanda[6] , R. Alfaro Molina[72] , B. Ali[17] , Y. Ali[15] , A. Alici[10,53,27] , A. Alkin[2] , J. Alme[22] , T. Alt[69] , L. Altenkamper[22] , I. Altsybeev[111] , M.N. Anaam[6] , C. Andrei[47] , D. Andreou[34] , H.A. Andrews[108] , A. Andronic[143,104] , M. Angeletti[34] , V. Anguelov[102] , C. Anson[16] , T. Antičić[105] , F. Antinori[56] , P. Antonioli[53] , R. Anwar[125] , N. Apadula[79] , L. Aphecetche[113] , H. Appelshäuser[69] , S. Arcelli[27] , R. Arnaldi[58] , M. Arratia[79] , I.C. Arsene[21] , M. Arslandok[102] , A. Augustinus[34] , R. Averbeck[104] , M.D. Azmi[17] , A. Badalà[55] , Y.W. Baek[40,60] , S. Bagnasco[58] , R. Bailhache[69] , R. Bala[99] , A. Baldisseri[136] , M. Ball[42] , R.C. Baral[85] , R. Barbera[28] , L. Barioglio[26] , G.G. Barnaföldi[144] , L.S. Barnby[92] , V. Barret[133] , P. Bartalini[6] , K. Barth[34] , E. Bartsch[69] , N. Bastid[133] , S. Basu[142] , G. Batigne[113] , B. Batyunya[75] , P.C. Batzing[21] , D. Bauri[48] , J.L. Bazo Alba[109] , I.G. Bearden[88] , C. Bedda[63] , N.K. Behera[60] , I. Belikov[135] , F. Bellini[34] , H. Bello Martinez[44] , R. Bellwied[125] , L.G.E. Beltran[119] , V. Belyaev[91] , G. Bencedi[144] , S. Beole[26] , A. Bercuci[47] , Y. Berdnikov[96] , D. Berenyi[144] , R.A. Bertens[129] , D. Berzano[58] , L. Betev[34] , A. Bhasin[99] , I.R. Bhat[99] , H. Bhatt[48] , B. Bhattacharjee[41] , A. Bianchi[26] , L. Bianchi[125,26] , N. Bianchi[51] , J. Bielčík[37] , J. Bielčíková[93] , A. Bilandzic[103,116] , G. Biro[144] , R. Biswas[3] , S. Biswas[3] , J.T. Blair[118] , D. Blau[87] , C. Blume[69] , G. Boca[138] , F. Bock[34] , A. Bogdanov[91] , L. Boldizsár[144] , A. Bolozdynya[91] , M. Bombara[38] , G. Bonomi[139] , M. Bonora[34] , H. Borel[136] , A. Borissov[143,102] , M. Borri[127] , E. Botta[26] , C. Bourjau[88] , L. Bratrud[69] , P. Braun-Munzinger[104] , M. Bregant[120] , T.A. Broker[69] , M. Broz[37] , E.J. Brucken[43] , E. Bruna[58] , G.E. Bruno[33] , M.D. Buckland[127] , D. Budnikov[106] , H. Buesching[69] , S. Bufalino[31] , P. Buhler[112] , P. Buncic[34] , O. Busch[132,i], Z. Buthelezi[73] , J.B. Butt[15] , J.T. Buxton[95] , D. Caffarri[89] , H. Caines[145] , A. Caliva[104] , E. Calvo Villar[109] , R.S. Camacho[44] , P. Camerini[25] , A.A. Capon[112] , F. Carnesecchi[10,27] , J. Castillo Castellanos[136] , A.J. Castro[129] , E.A.R. Casula[54] , C. Ceballos Sanchez[52] , P. Chakraborty[48] , S. Chandra[140] , B. Chang[126] , W. Chang[6] , S. Chapeland[34] , M. Chartier[127] , S. Chattopadhyay[140] , S. Chattopadhyay[107] , A. Chauvin[24] , C. Cheshkov[134] , B. Cheynis[134] , V. Chibante Barroso[34] , D.D. Chinellato[121] , S. Cho[60] , P. Chochula[34] , T. Chowdhury[133] , P. Christakoglou[89] , C.H. Christensen[88] , P. Christiansen[80] , T. Chujo[132] , C. Cicalo[54] , L. Cifarelli[10,27] , F. Cindolo[53] , J. Cleymans[124] , F. Colamaria[52] , D. Colella[52] , A. Collu[79] , M. Colocci[27] , M. Concas[58,ii], G. Conesa Balbastre[78] , Z. Conesa del Valle[61] , G. Contin[127] , J.G. Contreras[37] , T.M. Cormier[94] , Y. Corrales Morales[26,58] , P. Cortese[32] , M.R. Cosentino[122] , F. Costa[34] , S. Costanza[138] , J. Crkovská[61] , P. Crochet[133] , E. Cuautle[70] , L. Cunqueiro[94] , D. Dabrowski[141] , T. Dahms[103,116] , A. Dainese[56] , F.P.A. Damas[113,136] , S. Dani[66] , M.C. Danisch[102] , A. Danu[68] , D. Das[107] , I. Das[107] , S. Das[3] , A. Dash[85] , S. Dash[48] , A. Dashi[103] , S. De[85,49] , A. De Caro[30] , G. de Cataldo[52] , C. de Conti[120] , J. de Cuveland[39] , A. De Falco[24] , D. De Gruttola[10,30] , N. De Marco[58] , S. De Pasquale[30] , R.D. De Souza[121] , H.F. Degenhardt[120] , A. Deisting[104,102] , K.R. Deja[141] , A. Deloff[84] , S. Delsanto[26] , P. Dhankher[48] , D. Di Bari[33] , A. Di Mauro[34] , R.A. Diaz[8] , T. Dietel[124] , P. Dillenseger[69] , Y. Ding[6] , R. Divià[34] , Ø. Djuvsland[22] , A. Dobrin[34] , D. Domenicis Gimenez[120] , B. Dönigus[69] , O. Dordic[21] , A.K. Dubey[140] , A. Dubla[104] , S. Dudi[98] , A.K. Duggal[98] , M. Dukhishyam[85] , P. Dupieux[133] , R.J. Ehlers[145] , D. Elia[52] , H. Engel[74] , E. Epple[145] , B. Erazmus[113] , F. Erhardt[97] , A. Erokhin[111] , M.R. Ersdal[22] , B. Espagnon[61] , G. Eulisse[34] , J. Eum[18] , D. Evans[108] , S. Evdokimov[90] , L. Fabbietti[103,116] , M. Faggin[29] , J. Faivre[78] , A. Fantoni[51] , M. Fasel[94] , L. Feldkamp[143] , A. Feliciello[58] , G. Feofilov[111] , A. Fernández Téllez[44] , A. Ferrero[136] , A. Ferretti[26] , A. Festanti[34] , V.J.G. Feuillard[102] , J. Figiel[117] , S. Filchagin[106] , D. Finogeev[62] , F.M. Fionda[22] , G. Fiorenza[52] , F. Flor[125] , S. Foertsch[73] , P. Foka[104] , S. Fokin[87] , E. Fragiacomo[59] , A. Francisco[113] , U. Frankenfeld[104] , G.G. Fronze[26] , U. Fuchs[34] , C. Furget[78] , A. Furs[62] , M. Fusco Girard[30] , J.J. Gaardhøje[88] , M. Gagliardi[26] , A.M. Gago[109] , K. Gajdosova[88,37] , A. Gal[135] , C.D. Galvan[119] , P. Ganoti[83] , C. Garabatos[104] , E. Garcia-Solis[11] , K. Garg[28] , C. Gargiulo[34] , K. Garner[143] , P. Gasik[103,116] , E.F. Gauger[118] , M.B. Gay Ducati[71] , M. Germain[113] , J. Ghosh[107] , P. Ghosh[140] , S.K. Ghosh[3] , P. Gianotti[51] , P. Giubellino[104,58] , P. Giubilato[29] , P. Glässel[102] , D.M. Goméz Coral[72] , A. Gomez Ramirez[74] , V. Gonzalez[104] , P. González-Zamora[44] , S. Gorbunov[39] , L. Görlich[117] , S. Gotovac[35] , V. Grabski[72] , L.K. Graczykowski[141] , K.L. Graham[108] , L. Greiner[79] , A. Grelli[63] , C. Grigoras[34] , V. Grigoriev[91] , A. Grigoryan[1] , S. Grigoryan[75] , J.M. Gronefeld[104] , F. Grosa[31] , J.F. Grosse-Oetringhaus[34] , R. Grosso[104] , R. Guernane[78] , B. Guerzoni[27] , M. Guittiere[113] , K. Gulbrandsen[88] , T. Gunji[131] , A. Gupta[99] , R. Gupta[99] , I.B. Guzman[44] , R. Haake[145,34] , M.K. Habib[104] , C. Hadjidakis[61] , H. Hamagaki[81] , G. Hamar[144] , M. Hamid[6] , J.C. Hamon[135] , R. Hannigan[118] , M.R. Haque[63] , A. Harlenderova[104] , J.W. Harris[145] , A. Harton[11] , H. Hassan[78] , D. Hatzifotiadou[53,10] , P. Hauer[42] , S. Hayashi[131] , S.T. Heckel[69] , E. Hellbär[69] , H. Helstrup[36] , A. Herghelegiu[47] , E.G. Hernandez[44] , G. Herrera Corral[9] , F. Herrmann[143] , K.F. Hetland[36] , T.E. Hilden[43] , H. Hillemanns[34] , C. Hills[127] , B. Hippolyte[135] , B. Hohlweger[103] , D. Horak[37] , S. Hornung[104] , R. Hosokawa[132] , J. Hota[66] , P. Hristov[34] ,

C. Huang[61] , C. Hughes[129] , P. Huhn[69] , T.J. Humanic[95] , H. Hushnud[107] , L.A. Husova[143] , N. Hussain[41] , S.A. Hussain[15] , T. Hussain[17] , D. Hutter[39] , D.S. Hwang[19] , J.P. Iddon[127] , R. Ilkaev[106] , M. Inaba[132] , M. Ippolitov[87] , M.S. Islam[107] , M. Ivanov[104] , V. Ivanov[96] , V. Izucheev[90] , B. Jacak[79] , N. Jacazio[27] , P.M. Jacobs[79] , M.B. Jadhav[48] , S. Jadlovska[115] , J. Jadlovsky[115] , S. Jaelani[63] , C. Jahnke[120] , M.J. Jakubowska[141] , M.A. Janik[141] , M. Jercic[97] , O. Jevons[108] , R.T. Jimenez Bustamante[104] , M. Jin[125] , P.G. Jones[108] , A. Jusko[108] , P. Kalinak[65] , A. Kalweit[34] , J.H. Kang[146] , V. Kaplin[91] , S. Kar[6] , A. Karasu Uysal[77] , O. Karavichev[62] , T. Karavicheva[62] , P. Karczmarczyk[34] , E. Karpechev[62] , U. Kebschull[74] , R. Keidel[46] , M. Keil[34] , B. Ketzer[42] , Z. Khabanova[89] , A.M. Khan[6] , S. Khan[17] , S.A. Khan[140] , A. Khanzadeev[96] , Y. Kharlov[90] , A. Khatun[17] , A. Khuntia[49] , B. Kileng[36] , B. Kim[60] , B. Kim[132] , D. Kim[146] , D.J. Kim[126] , E.J. Kim[13] , H. Kim[146] , J.S. Kim[40] , J. Kim[102] , J. Kim[146] , J. Kim[13] , M. Kim[60,102] , S. Kim[19] , T. Kim[146] , T. Kim[146] , K. Kindra[98] , S. Kirsch[39] , I. Kisel[39] , S. Kiselev[64] , A. Kisiel[141] , J.L. Klay[5] , C. Klein[69] , J. Klein[58] , S. Klein[79] , C. Klein-Bösing[143] , S. Klewin[102] , A. Kluge[34] , M.L. Knichel[34] , A.G. Knospe[125] , C. Kobdaj[114] , M. Kofarago[144] , M.K. Köhler[102] , T. Kollegger[104] , A. Kondratyev[75] , N. Kondratyeva[91] , E. Kondratyuk[90] , P.J. Konopka[34] , M. Konyushikhin[142] , L. Koska[115] , O. Kovalenko[84] , V. Kovalenko[111] , M. Kowalski[117] , I. Králik[65] , A. Kravčáková[38] , L. Kreis[104] , M. Krivda[65,108] , F. Krizek[93] , M. Krüger[69] , E. Kryshen[96] , M. Krzewicki[39] , A.M. Kubera[95] , V. Kučera[93,60] , C. Kuhn[135] , P.G. Kuijer[89] , L. Kumar[98] , S. Kumar[48] , S. Kundu[85] , P. Kurashvili[84] , A. Kurepin[62] , A.B. Kurepin[62] , S. Kushpil[93] , J. Kvapil[108] , M.J. Kweon[60] , Y. Kwon[146] , S.L. La Pointe[39] , P. La Rocca[28] , Y.S. Lai[79] , R. Langoy[123] , K. Lapidus[34,145] , A. Lardeux[21] , P. Larionov[51] , E. Laudi[34] , R. Lavicka[37] , T. Lazareva[111] , R. Lea[25] , L. Leardini[102] , S. Lee[146] , F. Lehas[89] , S. Lehner[112] , J. Lehrbach[39] , R.C. Lemmon[92] , I. León Monzón[119] , P. Lévai[144] , X. Li[12] , X.L. Li[6] , J. Lien[123] , R. Lietava[108] , B. Lim[18] , S. Lindal[21] , V. Lindenstruth[39] , S.W. Lindsay[127] , C. Lippmann[104] , M.A. Lisa[95] , V. Litichevskyi[43] , A. Liu[79] , H.M. Ljunggren[80] , W.J. Llope[142] , D.F. Lodato[63] , V. Loginov[91] , C. Loizides[94] , P. Loncar[35] , X. Lopez[133] , E. López Torres[8] , P. Luettig[69] , J.R. Luhder[143] , M. Lunardon[29] , G. Luparello[59] , M. Lupi[34] , A. Maevskaya[62] , M. Mager[34] , S.M. Mahmood[21] , T. Mahmoud[42] , A. Maire[135] , R.D. Majka[145] , M. Malaev[96] , Q.W. Malik[21] , L. Malinina[75,iii], D. Mal'Kevich[64] , P. Malzacher[104] , A. Mamonov[106] , V. Manko[87] , F. Manso[133] , V. Manzari[52] , Y. Mao[6] , M. Marchisone[134] , J. Mareš[67] , G.V. Margagliotti[25] , A. Margotti[53] , J. Margutti[63] , A. Marín[104] , C. Markert[118] , M. Marquard[69] , N.A. Martin[104,102] , P. Martinengo[34] , J.L. Martinez[125] , M.I. Martínez[44] , G. Martínez García[113] , M. Martinez Pedreira[34] , S. Masciocchi[104] , M. Masera[26] , A. Masoni[54] , L. Massacrier[61] , E. Masson[113] , A. Mastroserio[52,137] , A.M. Mathis[103,116] , P.F.T. Matuoka[120] , A. Matyja[129,117] , C. Mayer[117] , M. Mazzilli[33] , M.A. Mazzoni[57] , F. Meddi[23] , Y. Melikyan[91] , A. Menchaca-Rocha[72] , E. Meninno[30] , M. Meres[14] , S. Mhlanga[124] , Y. Miake[132] , L. Micheletti[26] , M.M. Mieskolainen[43] , D.L. Mihaylov[103] , K. Mikhaylov[75,64] , A. Mischke[63,i], A.N. Mishra[70] , D. Miśkowiec[104] , C.M. Mitu[68] , N. Mohammadi[34] , A.P. Mohanty[63] , B. Mohanty[85] , M. Mohisin Khan[17,iv], M.M. Mondal[66] , C. Mordasini[103] , D.A. Moreira De Godoy[143] , L.A.P. Moreno[44] , S. Moretto[29] , A. Morreale[113] , A. Morsch[34] , T. Mrnjavac[34] , V. Muccifora[51] , E. Mudnic[35] , D. Mühlheim[143] , S. Muhuri[140] , M. Mukherjee[3] , J.D. Mulligan[145] , M.G. Munhoz[120] , K. Münning[42] , R.H. Munzer[69] , H. Murakami[131] , S. Murray[73] , L. Musa[34] , J. Musinsky[65] , C.J. Myers[125] , J.W. Myrcha[141] , B. Naik[48] , R. Nair[84] , B.K. Nandi[48] , R. Nania[53,10] , E. Nappi[52] , M.U. Naru[15] , A.F. Nassirpour[80] , H. Natal da Luz[120] , C. Nattrass[129] , S.R. Navarro[44] , K. Nayak[85] , R. Nayak[48] , T.K. Nayak[140,85] , S. Nazarenko[106] , R.A. Negrao De Oliveira[69] , L. Nellen[70] , S.V. Nesbo[36] , G. Neskovic[39] , F. Ng[125] , B.S. Nielsen[88] , S. Nikolaev[87] , S. Nikulin[87] , V. Nikulin[96] , F. Noferini[10,53] , P. Nomokonov[75] , G. Nooren[63] , J.C.C. Noris[44] , J. Norman[78] , A. Nyanin[87] , J. Nystrand[22] , M. Ogino[81] , A. Ohlson[102] , J. Oleniacz[141] , A.C. Oliveira Da Silva[120] , M.H. Oliver[145] , J. Onderwaater[104] , C. Oppedisano[58] , R. Orava[43] , A. Ortiz Velasquez[70] , A. Oskarsson[80] , J. Otwinowski[117] , K. Oyama[81] , Y. Pachmayer[102] , V. Pacik[88] , D. Pagano[139] , G. Paić[70] , P. Palni[6] , J. Pan[142] , A.K. Pandey[48] , S. Panebianco[136] , V. Papikyan[1] , P. Pareek[49] , J. Park[60] , J.E. Parkkila[126] , S. Parmar[98] , A. Passfeld[143] , S.P. Pathak[125] , R.N. Patra[140] , B. Paul[58] , H. Pei[6] , T. Peitzmann[63] , X. Peng[6] , L.G. Pereira[71] , H. Pereira Da Costa[136] , D. Peresunko[87] , G.M. Perez[8] , E. Perez Lezama[69] , V. Peskov[69] , Y. Pestov[4] , V. Petráček[37] , M. Petrovici[47] , R.P. Pezzi[71] , S. Piano[59] , M. Pikna[14] , P. Pillot[113] , L.O.D.L. Pimentel[88] , O. Pinazza[53,34] , L. Pinsky[125] , S. Pisano[51] , D.B. Piyarathna[125] , M. Płoskoń[79] , M. Planinic[97] , F. Pliquett[69] , J. Pluta[141] , S. Pochybova[144] , P.L.M. Podesta-Lerma[119] , M.G. Poghosyan[94] , B. Polichtchouk[90] , N. Poljak[97] , W. Poonsawat[114] , A. Pop[47] , H. Poppenborg[143] , S. Porteboeuf-Houssais[133] , V. Pozdniakov[75] , S.K. Prasad[3] , R. Preghenella[53] , F. Prino[58] , C.A. Pruneau[142] , I. Pshenichnov[62] , M. Puccio[26] , V. Punin[106] , K. Puranapanda[140] , J. Putschke[142] , R.E. Quishpe[125] , S. Ragoni[108] , S. Raha[3] , S. Rajput[99] , J. Rak[126] , A. Rakotozafindrabe[136] , L. Ramello[32] , F. Rami[135] , R. Raniwala[100] , S. Raniwala[100] , S.S. Räsänen[43] , B.T. Rascanu[69] , R. Rath[49] , V. Ratza[42] , I. Ravasenga[31] , K.F. Read[129,94] , K. Redlich[84,v], A. Rehman[22] , P. Reichelt[69] , F. Reidt[34] , X. Ren[6] , R. Renfordt[69] , A. Reshetin[62] , J.-P. Revol[10] , K. Reygers[102] , V. Riabov[96] , T. Richert[88,80] , M. Richter[21] , P. Riedler[34] , W. Riegler[34] , F. Riggi[28] , C. Ristea[68] , S.P. Rode[49] , M. Rodríguez Cahuantzi[44] , K. Røed[21] , R. Rogalev[90] , E. Rogochaya[75] , D. Rohr[34] , D. Röhrich[22] , P.S. Rokita[141] , F. Ronchetti[51] , E.D. Rosas[70] , K. Roslon[141] , P. Rosnet[133] , A. Rossi[56,29] , A. Rotondi[138] , F. Roukoutakis[83] , A. Roy[49] , P. Roy[107] , O.V. Rueda[80] , R. Rui[25] , B. Rumyantsev[75] , A. Rustamov[86] , E. Ryabinkin[87] , Y. Ryabov[96] , A. Rybicki[117] , S. Saarinen[43] , S. Sadhu[140] , S. Sadovsky[90] , K. Šafařík[34,37] , S.K. Saha[140] , B. Sahoo[48] , P. Sahoo[49] , R. Sahoo[49] , S. Sahoo[66] , P.K. Sahu[66] , J. Saini[140] , S. Sakai[132] , S. Sambyal[99] , V. Samsonov[96,91] , A. Sandoval[72] , A. Sarkar[73] , D. Sarkar[140] , N. Sarkar[140] , P. Sarma[41] , V.M. Sarti[103] , M.H.P. Sas[63] , E. Scapparone[53] , B. Schaefer[94] , J. Schambach[118] , H.S. Scheid[69] , C. Schiaua[47] , R. Schicker[102] , A. Schmah[102] , C. Schmidt[104] , H.R. Schmidt[101] , M.O. Schmidt[102] , M. Schmidt[101] , N.V. Schmidt[69,94] , A.R. Schmier[129] , J. Schukraft[88,34] , Y. Schutz[135,34] , K. Schwarz[104] , K. Schweda[104] , G. Scioli[27] , E. Scomparin[58] , M. Šefčík[38] , J.E. Seger[16] , Y. Sekiguchi[131] , D. Sekihata[45] , I. Selyuzhenkov[104,91] , S. Senyukov[135] , E. Serradilla[72] , P. Sett[48] , A. Sevcenco[68] , A. Shabanov[62] , A. Shabetai[113] , R. Shahoyan[34] , W. Shaikh[107] , A. Shangaraev[90] , A. Sharma[98] , A. Sharma[99] , M. Sharma[99] , N. Sharma[98] , A.I. Sheikh[140] , K. Shigaki[45] , M. Shimomura[82] , S. Shirinkin[64] , Q. Shou[6,110] , Y. Sibiriak[87] , S. Siddhanta[54] , T. Siemiarczuk[84] , D. Silvermyr[80] , G. Simatovic[89] , G. Simonetti[103,34] , R. Singh[85] , R. Singh[99] , V.K. Singh[140] , V. Singhal[140] , T. Sinha[107] , B. Sitar[14] , M. Sitta[32] , T.B. Skaali[21] , M. Slupecki[126] , N. Smirnov[145] , R.J.M. Snellings[63] , T.W. Snellman[126] , J. Sochan[115] , C. Soncco[109] , J. Song[60] , A. Songmoolnak[114] , F. Soramel[29] , S. Sorensen[129] , F. Sozzi[104] , I. Sputowska[117] , J. Stachel[102] , I. Stan[68] , P. Stankus[94] , E. Stenlund[80] , D. Stocco[113] , M.M. Storetvedt[36] , P. Strmen[14] , A.A.P. Suaide[120] , T. Sugitate[45] , C. Suire[61] , M. Suleymanov[15] , M. Suljic[34] , R. Sultanov[64] , M. Šumbera[93] , S. Sumowidagdo[50] , K. Suzuki[112] , S. Swain[66] , A. Szabo[14] , I. Szarka[14] , U. Tabassam[15] , J. Takahashi[121] , G.J. Tambave[22] , N. Tanaka[132] , S. Tang[6] , M. Tarhini[113] , M.G. Tarzila[47] , A. Tauro[34] , G. Tejeda Muñoz[44] , A. Telesca[34] , C. Terrevoli[29,125] , D. Thakur[49] , S. Thakur[140] , D. Thomas[118] , F. Thoresen[88] , R. Tieulent[134] , A. Tikhonov[62] , A.R. Timmins[125] , A. Toia[69] , N. Topilskaya[62] , M. Toppi[51] , S.R. Torres[119] , S. Tripathy[49] , T. Tripathy[48] , S. Trogolo[26] , G. Trombetta[33] , L. Tropp[38] , V. Trubnikov[2] , W.H. Trzaska[126] , T.P. Trzcinski[141] , B.A. Trzeciak[63] , T. Tsuji[131] , A. Tumkin[106] , R. Turrisi[56] , T.S. Tveter[21] , K. Ullaland[22] , E.N. Umaka[125] , A. Uras[134] , G.L. Usai[24] , A. Utrobicic[97] , M. Vala[38,115] , L. Valencia Palomo[44] , N. Valle[138] , N. van der Kolk[63] , L.V.R. van Doremalen[63] , J.W. Van Hoorne[34] , M. van Leeuwen[63] , P. Vande Vyvre[34] , D. Varga[144] , A. Vargas[44] , M. Vargyas[126] , R. Varma[48] , M. Vasileiou[83] , A. Vasiliev[87] , O. Vázquez Doce[116,103] , V. Vechernin[111] , A.M. Veen[63] , E. Vercellin[26] , S. Vergara Limón[44] , L. Vermunt[63] , R. Vernet[7] , R. Vértesi[144] , L. Vickovic[35] , J. Viinikainen[126] , Z. Vilakazi[130] , O. Villalobos Baillie[108] , A. Villatoro Tello[44] , G. Vino[52] , A. Vinogradov[87] , T. Virgili[30] , V. Vislavicius[88] , A. Vodopyanov[75] , B. Volkel[34] , M.A. Völkl[101] , K. Voloshin[64] , S.A. Voloshin[142] , G. Volpe[33] , B. von Haller[34] , I. Vorobyev[103,116] , D. Voscek[115] , J. Vrláková[38] , B. Wagner[22] , M. Wang[6] , Y. Watanabe[132] , M. Weber[112] , S.G. Weber[104] , A. Wegrzynek[34] , D.F. Weiser[102] , S.C. Wenzel[34] , J.P. Wessels[143] , U. Westerhoff[143] , A.M. Whitehead[124] , E. Widmann[112] , J. Wiechula[69] , J. Wikne[21] , G. Wilk[84] , J. Wilkinson[53] , G.A. Willems[143,34] , E. Willsher[108] , B. Windelband[102] , W.E. Witt[129] , Y. Wu[128] , R. Xu[6] , S. Yalcin[77] , K. Yamakawa[45] , S. Yang[22] , S. Yano[136] , Z. Yin[6] , H. Yokoyama[63] , I.-K. Yoo[18] , J.H. Yoon[60] , S. Yuan[22] , V. Yurchenko[2] , V. Zaccolo[58,25] , A. Zaman[15] , C. Zampolli[34] , H.J.C. Zanoli[120] , N. Zardoshti[34,108] , A. Zarochentsev[111] , P. Závada[67] , N. Zaviyalov[106] , H. Zbroszczyk[141] , M. Zhalov[96] , X. Zhang[6] , Y. Zhang[6] , Z. Zhang[6,133] , C. Zhao[21] , V. Zherebchevskii[111] , N. Zhigareva[64] , D. Zhou[6] , Y. Zhou[88] , Z. Zhou[22] , H. Zhu[6] , J. Zhu[6] , Y. Zhu[6] , A. Zichichi[27,10] , M.B. Zimmermann[34] , G. Zinovjev[2] , N. Zurlo[139] ,

Affiliation notes

[i] Deceased
[ii] Dipartimento DET del Politecnico di Torino, Turin, Italy
[iii] M.V. Lomonosov Moscow State University, D.V. Skobeltsyn Institute of Nuclear, Physics, Moscow, Russia
[iv] Department of Applied Physics, Aligarh Muslim University, Aligarh, India
[v] Institute of Theoretical Physics, University of Wroclaw, Poland

Collaboration Institutes

[1] A.I. Alikhanyan National Science Laboratory (Yerevan Physics Institute) Foundation, Yerevan, Armenia
[2] Bogolyubov Institute for Theoretical Physics, National Academy of Sciences of Ukraine, Kiev, Ukraine
[3] Bose Institute, Department of Physics and Centre for Astroparticle Physics and Space Science (CAPSS), Kolkata, India
[4] Budker Institute for Nuclear Physics, Novosibirsk, Russia
[5] California Polytechnic State University, San Luis Obispo, California, United States
[6] Central China Normal University, Wuhan, China

[7] Centre de Calcul de l'IN2P3, Villeurbanne, Lyon, France
[8] Centro de Aplicaciones Tecnológicas y Desarrollo Nuclear (CEADEN), Havana, Cuba
[9] Centro de Investigación y de Estudios Avanzados (CINVESTAV), Mexico City and Mérida, Mexico
[10] Centro Fermi - Museo Storico della Fisica e Centro Studi e Ricerche "Enrico Fermi', Rome, Italy
[11] Chicago State University, Chicago, Illinois, United States
[12] China Institute of Atomic Energy, Beijing, China
[13] Chonbuk National University, Jeonju, Republic of Korea
[14] Comenius University Bratislava, Faculty of Mathematics, Physics and Informatics, Bratislava, Slovakia
[15] COMSATS Institute of Information Technology (CIIT), Islamabad, Pakistan
[16] Creighton University, Omaha, Nebraska, United States
[17] Department of Physics, Aligarh Muslim University, Aligarh, India
[18] Department of Physics, Pusan National University, Pusan, Republic of Korea
[19] Department of Physics, Sejong University, Seoul, Republic of Korea
[20] Department of Physics, University of California, Berkeley, California, United States
[21] Department of Physics, University of Oslo, Oslo, Norway
[22] Department of Physics and Technology, University of Bergen, Bergen, Norway
[23] Dipartimento di Fisica dell'Università 'La Sapienza' and Sezione INFN, Rome, Italy
[24] Dipartimento di Fisica dell'Università and Sezione INFN, Cagliari, Italy
[25] Dipartimento di Fisica dell'Università and Sezione INFN, Trieste, Italy
[26] Dipartimento di Fisica dell'Università and Sezione INFN, Turin, Italy
[27] Dipartimento di Fisica e Astronomia dell'Università and Sezione INFN, Bologna, Italy
[28] Dipartimento di Fisica e Astronomia dell'Università and Sezione INFN, Catania, Italy
[29] Dipartimento di Fisica e Astronomia dell'Università and Sezione INFN, Padova, Italy
[30] Dipartimento di Fisica 'E.R. Caianiello' dell'Università and Gruppo Collegato INFN, Salerno, Italy
[31] Dipartimento DISAT del Politecnico and Sezione INFN, Turin, Italy
[32] Dipartimento di Scienze e Innovazione Tecnologica dell'Università del Piemonte Orientale and INFN Sezione di Torino, Alessandria, Italy
[33] Dipartimento Interateneo di Fisica 'M. Merlin' and Sezione INFN, Bari, Italy
[34] European Organization for Nuclear Research (CERN), Geneva, Switzerland
[35] Faculty of Electrical Engineering, Mechanical Engineering and Naval Architecture, University of Split, Split, Croatia
[36] Faculty of Engineering and Science, Western Norway University of Applied Sciences, Bergen, Norway
[37] Faculty of Nuclear Sciences and Physical Engineering, Czech Technical University in Prague, Prague, Czech Republic
[38] Faculty of Science, P.J. Šafárik University, Košice, Slovakia
[39] Frankfurt Institute for Advanced Studies, Johann Wolfgang Goethe-Universität Frankfurt, Frankfurt, Germany
[40] Gangneung-Wonju National University, Gangneung, Republic of Korea
[41] Gauhati University, Department of Physics, Guwahati, India
[42] Helmholtz-Institut für Strahlen- und Kernphysik, Rheinische Friedrich-Wilhelms-Universität Bonn, Bonn, Germany
[43] Helsinki Institute of Physics (HIP), Helsinki, Finland
[44] High Energy Physics Group, Universidad Autónoma de Puebla, Puebla, Mexico
[45] Hiroshima University, Hiroshima, Japan
[46] Hochschule Worms, Zentrum für Technologietransfer und Telekommunikation (ZTT), Worms, Germany
[47] Horia Hulubei National Institute of Physics and Nuclear Engineering, Bucharest, Romania
[48] Indian Institute of Technology Bombay (IIT), Mumbai, India
[49] Indian Institute of Technology Indore, Indore, India
[50] Indonesian Institute of Sciences, Jakarta, Indonesia
[51] INFN, Laboratori Nazionali di Frascati, Frascati, Italy
[52] INFN, Sezione di Bari, Bari, Italy
[53] INFN, Sezione di Bologna, Bologna, Italy
[54] INFN, Sezione di Cagliari, Cagliari, Italy
[55] INFN, Sezione di Catania, Catania, Italy
[56] INFN, Sezione di Padova, Padova, Italy
[57] INFN, Sezione di Roma, Rome, Italy

[58] INFN, Sezione di Torino, Turin, Italy
[59] INFN, Sezione di Trieste, Trieste, Italy
[60] Inha University, Incheon, Republic of Korea
[61] Institut de Physique Nucléaire d'Orsay (IPNO), Institut National de Physique Nucléaire et de Physique des Particules (IN2P3/CNRS), Université de Paris-Sud, Université Paris-Saclay, Orsay, France
[62] Institute for Nuclear Research, Academy of Sciences, Moscow, Russia
[63] Institute for Subatomic Physics, Utrecht University/Nikhef, Utrecht, Netherlands
[64] Institute for Theoretical and Experimental Physics, Moscow, Russia
[65] Institute of Experimental Physics, Slovak Academy of Sciences, Košice, Slovakia
[66] Institute of Physics, Homi Bhabha National Institute, Bhubaneswar, India
[67] Institute of Physics of the Czech Academy of Sciences, Prague, Czech Republic
[68] Institute of Space Science (ISS), Bucharest, Romania
[69] Institut für Kernphysik, Johann Wolfgang Goethe-Universität Frankfurt, Frankfurt, Germany
[70] Instituto de Ciencias Nucleares, Universidad Nacional Autónoma de México, Mexico City, Mexico
[71] Instituto de Física, Universidade Federal do Rio Grande do Sul (UFRGS), Porto Alegre, Brazil
[72] Instituto de Física, Universidad Nacional Autónoma de México, Mexico City, Mexico
[73] iThemba LABS, National Research Foundation, Somerset West, South Africa
[74] Johann-Wolfgang-Goethe Universität Frankfurt Institut für Informatik, Fachbereich Informatik und Mathematik, Frankfurt, Germany
[75] Joint Institute for Nuclear Research (JINR), Dubna, Russia
[76] Korea Institute of Science and Technology Information, Daejeon, Republic of Korea
[77] KTO Karatay University, Konya, Turkey
[78] Laboratoire de Physique Subatomique et de Cosmologie, Université Grenoble-Alpes, CNRS-IN2P3, Grenoble, France
[79] Lawrence Berkeley National Laboratory, Berkeley, California, United States
[80] Lund University Department of Physics, Division of Particle Physics, Lund, Sweden
[81] Nagasaki Institute of Applied Science, Nagasaki, Japan
[82] Nara Women's University (NWU), Nara, Japan
[83] National and Kapodistrian University of Athens, School of Science, Department of Physics , Athens, Greece
[84] National Centre for Nuclear Research, Warsaw, Poland
[85] National Institute of Science Education and Research, Homi Bhabha National Institute, Jatni, India
[86] National Nuclear Research Center, Baku, Azerbaijan
[87] National Research Centre Kurchatov Institute, Moscow, Russia
[88] Niels Bohr Institute, University of Copenhagen, Copenhagen, Denmark
[89] Nikhef, National institute for subatomic physics, Amsterdam, Netherlands
[90] NRC Kurchatov Institute IHEP, Protvino, Russia
[91] NRNU Moscow Engineering Physics Institute, Moscow, Russia
[92] Nuclear Physics Group, STFC Daresbury Laboratory, Daresbury, United Kingdom
[93] Nuclear Physics Institute of the Czech Academy of Sciences, Řež u Prahy, Czech Republic
[94] Oak Ridge National Laboratory, Oak Ridge, Tennessee, United States
[95] Ohio State University, Columbus, Ohio, United States
[96] Petersburg Nuclear Physics Institute, Gatchina, Russia
[97] Physics department, Faculty of science, University of Zagreb, Zagreb, Croatia
[98] Physics Department, Panjab University, Chandigarh, India
[99] Physics Department, University of Jammu, Jammu, India
[100] Physics Department, University of Rajasthan, Jaipur, India
[101] Physikalisches Institut, Eberhard-Karls-Universität Tübingen, Tübingen, Germany
[102] Physikalisches Institut, Ruprecht-Karls-Universität Heidelberg, Heidelberg, Germany
[103] Physik Department, Technische Universität München, Munich, Germany
[104] Research Division and ExtreMe Matter Institute EMMI, GSI Helmholtzzentrum für Schwerionenforschung GmbH, Darmstadt, Germany
[105] Rudjer Bošković Institute, Zagreb, Croatia
[106] Russian Federal Nuclear Center (VNIIEF), Sarov, Russia
[107] Saha Institute of Nuclear Physics, Homi Bhabha National Institute, Kolkata, India
[108] School of Physics and Astronomy, University of Birmingham, Birmingham, United Kingdom

[109] Sección Física, Departamento de Ciencias, Pontificia Universidad Católica del Perú, Lima, Peru
[110] Shanghai Institute of Applied Physics, Shanghai, China
[111] St. Petersburg State University, St. Petersburg, Russia
[112] Stefan Meyer Institut für Subatomare Physik (SMI), Vienna, Austria
[113] SUBATECH, IMT Atlantique, Université de Nantes, CNRS-IN2P3, Nantes, France
[114] Suranaree University of Technology, Nakhon Ratchasima, Thailand
[115] Technical University of Košice, Košice, Slovakia
[116] Technische Universität München, Excellence Cluster 'Universe', Munich, Germany
[117] The Henryk Niewodniczanski Institute of Nuclear Physics, Polish Academy of Sciences, Cracow, Poland
[118] The University of Texas at Austin, Austin, Texas, United States
[119] Universidad Autónoma de Sinaloa, Culiacán, Mexico
[120] Universidade de São Paulo (USP), São Paulo, Brazil
[121] Universidade Estadual de Campinas (UNICAMP), Campinas, Brazil
[122] Universidade Federal do ABC, Santo Andre, Brazil
[123] University College of Southeast Norway, Tonsberg, Norway
[124] University of Cape Town, Cape Town, South Africa
[125] University of Houston, Houston, Texas, United States
[126] University of Jyväskylä, Jyväskylä, Finland
[127] University of Liverpool, Liverpool, United Kingdom
[128] University of Science and Techonology of China, Hefei, China
[129] University of Tennessee, Knoxville, Tennessee, United States
[130] University of the Witwatersrand, Johannesburg, South Africa
[131] University of Tokyo, Tokyo, Japan
[132] University of Tsukuba, Tsukuba, Japan
[133] Université Clermont Auvergne, CNRS/IN2P3, LPC, Clermont-Ferrand, France
[134] Université de Lyon, Université Lyon 1, CNRS/IN2P3, IPN-Lyon, Villeurbanne, Lyon, France
[135] Université de Strasbourg, CNRS, IPHC UMR 7178, F-67000 Strasbourg, France, Strasbourg, France
[136] Université Paris-Saclay Centre dÉtudes de Saclay (CEA), IRFU, Department de Physique Nucléaire (DPhN), Saclay, France
[137] Università degli Studi di Foggia, Foggia, Italy
[138] Università degli Studi di Pavia, Pavia, Italy
[139] Università di Brescia, Brescia, Italy
[140] Variable Energy Cyclotron Centre, Homi Bhabha National Institute, Kolkata, India
[141] Warsaw University of Technology, Warsaw, Poland
[142] Wayne State University, Detroit, Michigan, United States
[143] Westfälische Wilhelms-Universität Münster, Institut für Kernphysik, Münster, Germany
[144] Wigner Research Centre for Physics, Hungarian Academy of Sciences, Budapest, Hungary
[145] Yale University, New Haven, Connecticut, United States
[146] Yonsei University, Seoul, Republic of Korea